Revision 1

Constraints on scheelite genesis at the Dabaoshan stratabound polymetallic deposit, South China

SHI-QIANG SU[1,2,3,4], KE-ZHANG QIN[1,2,3,*], GUANG-MING LI[1,2,3], ROSS R. LARGE[4], PAUL OLIN[4], AND NOREEN J. EVANS[5]

[1]Key Laboratory of Mineral Resources, Institute of Geology and Geophysics, Chinese Academy of Sciences, Beijing 100029, China

[2]Innovation Academy for Earth Science, Chinese Academy of Sciences, Beijing 100029, China

[3]University of Chinese Academy of Sciences, Beijing 100049, China

[4]Centre for Ore Deposit and Earth Sciences (CODES), School of Nature Sciences, University of Tasmania, Hobart, Tasmania 7001, Australia

[5]School of Earth and Planetary Sciences, John de Laeter Center, Curtin University, Bentley 6845, Australia

*Corresponding author: Ke-Zhang Qin; Email: kzq@mail.iggcas.ac.cn

ABSTRACT

The genesis of the Dabaoshan stratabound base metal deposit has remained in dispute since its discovery. Scheelite is commonly present in both the Cu-S orebody and adjacent porphyry-style Mo-W mineralization and can provide insights into the hydrothermal history. In the stratabound Cu-S orebodies, there are three stages of mineralization: early-stage, Cu-(W), and late-stage. Two types of scheelite (here referred to as SchA and SchB), are identified in the Cu-(W) mineralization stage. SchA is anhedral and disseminated in massive sulfide ores. It coexists with chalcopyrite and replaces the preexisting arsenic-bearing pyrite. SchA exhibits chaotic cathodoluminescent (CL) textures and contains abundant mineral inclusions, including pyrite, chalcopyrite, arsenopyrite, uraninite, and minor REE-bearing minerals. Chemically, SchA displays middle REE (MREE)-enriched patterns with negative Eu anomalies. SchB occurs in veins crosscutting the stratabound orebodies and shows patchy textures in CL images. Based on CL texture, SchB is subdivided into SchB1 and SchB2. SchB1 is CL-dark and occasionally shows oscillatory zoning, whereas SchB2 is CL-bright and relatively homogeneous. Chemically, SchB1 has a high U content (mean=552 ppm) and REE patterns varying from MREE-enriched to MREE-depleted. In contrast, SchB2 is depleted in U (mean=2.5 ppm) and has MREE-enriched patterns. Compared with SchB, SchA is significantly enriched in Ba.

Scheelite in the stratabound orebodies has a similar Y/Ho ratios and trace element characteristics as Sch3 in the Dabaoshan porphyry system. *In situ* U-Pb dating of hydrothermal apatite, collected from the Sch3-bearing veins in the footwall of stratabound orebodies, yielded a mineralization age of 160.8 ± 1.1 Ma. Zircon from the Dabaoshan granite porphyry yielded a U-Pb age of 161.8 ± 1.0 Ma. These two ages are

consistent within uncertainty, suggesting that the ore-forming fluid responsible for tungsten mineralization in the stratabound orebodies was derived from the porphyry system. When fluid emanating from the deep porphyry system encountered the overlying Lower Qiziqiao Formation and stratabound orebodies, replacement reactions resulted in dramatic variations in physiochemical conditions (e.g. decrease in fO_2, increase in Ca/Fe, As, Ba). During this process, $U^{6+}$was reduced to U^{4+}, and As and Ba were leached out of the preexisting pyrite and host rock. Fluid-rock interaction triggered a rapid discharge of fluids, forming SchA with chaotic CL textures and abundant inclusions, but uniform REE patterns. SchB (characterized by patches with different chemical characteristics) may have been formed from repeated injection of ascending fluids into fractures crosscutting the preexisting massive sulfide ores. We propose that Jurassic porphyry Mo-W mineralization contributed to tungsten mineralization in the stratabound orebodies. Considering that Cu and W mineralization are genetically related, not only in the footwall but also in the stratabound orebodies, we infer that Cu in the stratabound orebodies was locally sourced from the Jurassic porphyry mineralization.

Keywords

Scheelite, Trace elements, Stratabound mineralization, Dabaoshan, Apatite U-Pb dating

INTRODUCTION

Stratabound polymetallic deposits, an important reserve of base metals in South China, are widespread in the Lower Yangtze Region and the Cathaysia Block (Gu et al. 2007; Zaw et al. 2007; Mao et al. 2011b). These deposits are commonly hosted within Late Paleozoic carbonate units and distributed around Mesozoic intermediate-acid

magmatic rocks (Gu et al. 2007). Despite being extensively studied, the genesis of these deposits remains controversial, with views broadly falling into two groups: (1) these deposits were associated with the Mesozoic porphyry-skarn systems (e.g., Pan and Dong 1999; Mao et al. 2011b; Pirajno and Zhou 2015); (2) mineralization was related to Paleozoic volcanic-exhalative massive sulfide deposits being overprinted by Mesozoic magmatic-hydrothermal events (e.g., Ge and Han 1986; Gu et al. 2007). In recent years, the genesis of stratabound deposits in the Lower Yangtze Region has been well-studied (e.g., Cao et al. 2017; Zhang et al. 2017; Li et al. 2018a), but the formation of these deposits in the Cathaysia Block is poorly understood.

Metal components of stratabound polymetallic deposits in the Cathaysia Block are dominated by Pb, Zn, and Cu. Notably, W, mainly occurring as scheelite, serves as a characteristic metal component in many stratabound polymetallic deposits, such as Dabaoshan, Dongxiang, Yongping, and Yushui (Gu et al. 2007, and reference therein). Scheelite ($CaWO_4$) can incorporate a diversity of trace elements into its crystal lattice (e.g., Nassau and Loiacono 1963; Klein and Hurlbut 1993). Differences in composition of fluid, and/or conditions of precipitation, can result in variations in scheelite geochemical composition and cathodoluminescent textures (e.g., Song et al. 2014; Poulin et al. 2016; Su et al. 2019a). Based on cathodoluminescence (CL) imaging, targeted *in situ* trace element analysis of scheelite can reveal these subtle variations and provide critical information about scheelite growth history and hydrothermal evolution (e.g., Brugger et al. 2000; Song et al. 2014; Li et al. 2018b; Su et al. 2019a). Thus, scheelite in stratabound polymetallic deposit could provide a better geochemical record of ore-forming processes.

In this context, the Dabaoshan district (Nanling Region, South China), provides an ideal natural laboratory in which to apply scheelite chemistry to elucidate the genesis

of tungsten mineralization in stratabound ore deposits. The Dabaoshan ore district contains typical porphyry-skarn Mo-W mineralization genetically related to the Jurassic granite porphyry and the adjacent stratabound Cu-Zn-Pb mineralization hosted in the Devonian strata (Wang et al. 2011; Mao et al. 2017). At Dabaoshan, scheelite is present not only in the porphyry-style veinlet mineralization, but also in the stratabound orebodies. Based on CL textures and trace element signatures, Su et al. (2019a) reported that scheelite in the Dabaoshan porphyry Mo-W mineralization can be divided into three generations (Sch1–Sch3). From early to late generations, scheelite is gradually depleted in Mo, Nb, Ta, and V, but enriched in U and Th. The variations of trace element in scheelite lay a solid foundation for us to further investigate the genesis of scheelite in stratabound orebodies and cast light on the genetic relationship between stratabound orebodies and the porphyry system.

This study focuses on scheelite in stratabound orebodies. Petrographic observation utilized transmitted light, back-scattered electron imaging (BSE), X-ray fluorescence (XRF) mapping, and cathodoluminescence (CL). Major and trace element analysis of scheelite was performed using electron microprobe analyses (EMPA) and laser ablation-inductively coupled plasma-mass spectrometry (LA-ICP-MS), respectively. We also conducted *in situ* LA-ICP-MS U-Pb dating on zircon and hydrothermal apatite to constrain the genesis of scheelite-bearing veins in the footwall of stratabound orebodies. By integrating these datasets, this study aims to decipher the genesis of scheelite in stratabound orebodies and cast light on the genetic relationship between these orebodies and the porphyry Mo-W mineralization at Dabaoshan.

GEOLOGICAL SETTING

The Nanling Region is located in the interior of the South China Block (SCB). The

SCB comprises the Cathaysia Block to the southeast and Yangtze Block to the northwest (Fig. 1), which amalgamated during the early Neoproterozoic (Charvet et al. 1996; Li et al. 1995). From the early Paleozoic to late Mesozoic, the whole SCB underwent three major orogenies, known as the Early Paleozoic Orogeny, the Early Mesozoic Orogeny, and the Late Mesozoic Orogeny (Wang et al. 2013; Zhou et al. 2006; Mao et al. 2013a). The Late Mesozoic (Jurassic-Cretaceous) orogeny resulted in widespread granite magmatism (Zhou et al. 2006) and related W-Sn and U mineralization in the Nanling Region (Hu et al. 2008; Mao et al. 2011a). Although less abundant than W-Sn, several important Mesozoic Cu and Mo deposits have been discovered in this area (Mao et al. 2013a). Previous studies suggested that tungsten mineralization in the Nanling Region mainly occurred at 155–165 Ma and is genetically related to the Jurassic granites (Mao et al. 2013a; Zhao et al. 2017). A variety of tectonic models have been proposed to interpret the large-scale Mesozoic magmatism and mineralization in this region, including (1) an active centennial margin related to the subduction of Pacific plate (e.g., Zhou and Li, 2000; Zhou et al. 2006; Li and Li, 2007; Sun et al. 2007) and (2) asthenospheric upwelling during intraplate lithospheric extension (e.g., Hsü et al., 1990). The Dabaoshan district, one of the biggest polymetallic ore districts in the Nanling Region (Wang et al. 2011; Mao et al. 2017; Su et al. 2019b), occurs on the intersection between the EW-trending Dadongshan-Guidong tectono-magmatic belt and the NE-trending Wuchuan-Sihui Fault in Nanling Region (Fig. 1a).

Strata and magmatic rocks

Exposed strata in the Dabaoshan district consists of Cambrian, Devonian, and Lower Jurassic sedimentary rocks (Fig. 1b). The Cambrian Gaotan Formation, exposed

in the north-west part of the district, comprises meta-sandstone, siltstone, sericitic shale, and argillaceous limestone. The Devonian sequences include the Lower-Middle Devonian Laohutou Formation, Middle Devonian Qiziqiao Formation, and Upper Devonian Tianziling Formation. The Laohutou Formation consists mainly of pale-grey sandstone, siltstone, and shale, with conglomerate at the base. The Qiziqiao Formation is divided into the Upper and Lower sub-formations: The Upper Qiziqiao Formation comprises pale-green shale, mudstone, tuffs, and volcanic breccias while the Lower Qiziqiao Formation (host to the stratabound Cu-Zn-Pb orebodies (Fig. 2); Ge and Han 1986; Wang et al. 2011) consists of dolomitic limestone, carbonaceous and calcareous mudstone, dolomitic and calcitic sandy shale. The Tianziling Formation, exposed in the western part of the district, comprises moderate- to thickly-layered micritic limestone intercalated with thin layers of silty limestone, massive chert-bearing limestone, and dolomitic limestone. The Jurassic Jinji Formation consists of graywackes intercalated with sericitic shale and coal beds.

Igneous rocks in Dabaoshan district include the Jurassic porphyries and Silurian volcanic rocks, with subordinate diabase dykes. The Jurassic porphyry, intruding along an E-W-trending fault, was offset by the NNE-trending fault and divided into the Chuandu porphyritic granite and the Dabaoshan granite porphyry (Fig. 1b). The granite porphyry contains K-feldspar, plagioclase, quartz, muscovite, biotite, with minor fluorapatite, zircon, rutile, magnetite, and sphene (Huang et al. 2017). Whole-rock major-element geochemistry demonstrates that the Dabaoshan granite porphyry belongs to the high-K calc-alkaline and shoshonite series while whole-rock Sr-Nd and zircon Hf isotope signatures suggest that the granite porphyry originated from partial melting of the crystalline basement in the Cathaysia Block (Huang et al. 2017). Zircon U-Pb geochronological studies suggest that Dabaoshan and Chuandu were emplaced

synchronously, but published crystallization ages reported vary from 160 to 167 Ma (Li et al. 2012; Mao et al. 2013b; Wang et al. 2019). Silurian volcanic rocks are exposed widely in the Dabaoshan district, primarily along the ENE- and NNW-trending faults, cropping out at Jiuquling, Qiuba, Dabaoshan Ridge, and Xuwu (Fig. 1b). The layered volcanic rocks beneath the Lahutou Formation mainly comprise dacite, dacitic ignimbrite, volcanic brecccia, and tuffaceous sandstone (Wu et al. 2014; Su et al. 2019b). Zircon U-Pb geochronological studies yield ages ranging from 434 to 441Ma, indicating an early Silurian crystallization age (Wu et al. 2014; Su et al. 2019b; Wang et al. 2019).

Mineralization and alteration

Mineralization in the Dabaoshan district can be divided into four main types: (1) porphyry Mo-W; (2) skarn W-Mo; (3) stratabound Cu-Zn-Pb; and (4) supergene weathered gossan (Ge and Han 1986; Huang et al. 1987; Huang et al. 2017; Mao et al. 2017).

The Dabaoshan porphyry Mo-W deposit is characterized by veinlet-disseminated mineralization. Detailed description of veins and alteration can be found in Mao et al. (2017) and Su et al. (2019a) and is only briefly summarized here. Mo mineralization, occurring as quartz-molybdenite veins, is restricted to contacts between the Dabaoshan granite porphyry and the Silurian dacite (Fig. 1). Molybdenite Re-Os dates reported by many authors range from 163.2 ± 2.3 to 166.6 ± 0.8 Ma (Wang et al. 2011; Li et al. 2012; Pan et al. 2018). Tungsten mineralization, occurring as scheelite, can be divided into disseminated-type ores and vein-type ores. Disseminated scheelite is present

mainly in the Dabaoshan granite porphyry and is accompanied by strong muscovite alteration. The spatial distribution of scheelite-bearing veins is more extensive than that of disseminated-type scheelite ores, with the former extending from the Dabaoshan porphyry into the adjacent Devonian strata (Fig. 2). From the bottom upward and from proximal to distal, vein-type mineralization exhibits notable metal zoning (Fig. 2) (Mao et al. 2017; Su et al. 2019a), varying from quartz-molybdenite veins (V1), quartz-pyrite±scheelite veins (V2), and quartz-pyrite-chalcopyrite-scheelite veins (V3), to quartz-pyrite-sphalerite-galena veins (V4). Alteration changes from potassic alteration (K-feldspar, muscovite) to sericitic, and then to propylitic, with minor argillic alteration developed in late-stage veins (Huang et al. 2017; Mao et al. 2017).

Skarn-type W-Mo mineralization mainly occurs at the contact between the Chuandu pluton and the Tianziling limestone (Fig. 1b). The garnet skarn zones extend more than 2 km from west to east, with thickness ranging from 40 to 100 m. The porphyry- and skarn-type Mo-W ores contain 52,000 metric tons (t) of Mo metal and 45,000 t of WO_3 at grades of 0.07–1.77 wt % (Mao et al. 2017).

The stratabound Cu-Zn-Pb orebodies (stratiform, sub-stratiform or lenticular), are chiefly situated in the syncline of the Lower Qiziqiao Formation, to the east of the Dabaoshan Ridge dacite. They contain 0.86 Mt Cu@ 0.86%, 0.31Mt Pb@ 1.77 %, and 0.85Mt Zn@ 4.44%, respectively (Ge and Han 1986; Wang et al. 2011; Mao et al. 2017). The Cu-Zn-Pb mineralization consists of 33 orebodies, which extend laterally along NS-strike for 3.1 km and dip SEE, with thickness decreasing from north to south and from west to east (Ge and Han 1986). Orebody No.1 is the largest (2650 m long, 350

m wide, and 55 m thick on average) and accounts for 94% of the Cu reserves in this deposit. Orebodies can be further divided into Cu-S- and Pb-Zn-rich facies. The Cu-S-rich facies occur in the northern part of the district, adjacent to the Dabaoshan porphyry and comprise chalcopyrite, pyrrhotite, and pyrite (Fig. 3). Scheelite, present as fine grains (Figs. 4 and 5), mainly occurs in the Cu-S-rich portions of the stratabound orebodies. The Pb-Zn-rich facies is present in the southern part of the deposit (Fig. 2) and is composed mainly of galena and sphalerite, with minor colloform pyrite. Alteration minerals associated with stratabound orebodies include quartz, phlogopite, calcite, fluorite, talc, sericite, and quartz.

Below the stratabound orebody, there are massive stockworks, which used to be viewed as fluid conduits for a submarine exhalative system (Ge and Han 1986). These veins, with narrow (<1 cm) sericitization and silicification selvages on the edges, commonly crosscut the Lahutou Formation sandstone and the Silurian dacite and are nearly perpendicular to the stratabound orebodies. Notably, veins in the northern part of the deposits comprise pyrite, chalcopyrite, and quartz, with minor scheelite and apatite, whereas veins in the southern part of the deposits are composed mainly of pyrite and quartz. In the hanging wall of the stratabound orebodies, galena-sphalerite veins are locally present (Fig. 2). These veins show weak marbleization.

On the surface, substratiform and lenses of supergene weathered gossan (Fig. 1) are noted, with thickness ranging from 50 to 60 m. This gossan hosts 11 Mt of Fe with an average grade of 48.2 wt.% and mainly comprises limonite and goethite, with minor hematite, magnetite, wolframite, siderite, and malachite. Sulfide relicts of sphalerite,

pyrite, galena and chalcopyrite, are also locally present, indicating that the gossan may have resulted from weathering of stratabound Cu-Zn-Pb orebodies (Dai et al. 2015).

SAMPLING AND ANALYTICAL METHODS

Samples

Samples examined in this study were collected from eight recent (2013–2015) drillholes that form a NS-trending cross-section adjacent to the Dabaoshan porphyry (ca. 1.5 km) (Fig. 1). Despite the fact that the Jurassic porphyry was not intersected on this section, veinlet-type mineralization is ubiquitous and varies from V1 to V4, from deep to shallow levels (Fig. 2). Two substratiform Cu-S-rich orebodies in the Lower Qiziqiao Formation were intersected (Fig. 2) and four representative scheelite-bearing samples were collected for mapping and *in situ* analyses. Sample location is illustrated in Figure 2. In addition, one rock sample (DB-1) representing the Dabaoshan granite porphyry was collected for zircon U-Pb dating, and a quartz-pyrite-chalcopyrite-scheelite-apatite vein (7902-842) was collected for apatite U-Pb dating from the footwall of the stratabound orebody. Sample locations are marked on Figure 1.

M4 tornado X-ray fluorescence (XRF) images

Drill core samples were cut along the largest surfaces and polished for microbeam XRF mapping. The mapped areas ranged from 15 to 25 cm^2. XRF images were collected on a desktop microbeam X-ray fluorescence M4 Tornado instrument, equipped with a rhodium target X-ray tube operating at 50 kV and 500 nA and an XFlash silicon drift X-ray detector, at the Key Laboratory of Deep Oil and Gas, China

University of Petroleum. Maps were obtained using a 40-μm spot size and a 40-μm raster with dwell times of 10 ms per pixel.

Cathodoluminescence (CL)

All thin sections were finely polished and coated with carbon before analysis. Panchromatic SEM-CL images were collected using Nova Nano SEM 450 with a Gatan Mono CL4 detector installed on a Carl Zeiss SUPRA 55 SAPPHIRE field emission electron microscope, with beam current 6 nA and acceleration voltage of 10 kV, at the Institute of Geology and Geophysics, Chinese Academy of Sciences (IGGCAS).

EMPA spot analyses

EMPA quantitative spot analyses were conducted on a JEOL JXA-8503 Plus electron microprobe equipped with five tunable wavelength dispersive spectrometers in the Central Science Laboratory at University of Tasmania (UTAS). Operating conditions were 40° takeoff angle, with beam energy of 20 kV. A probe current of 120 nA and a 2 μm diameter size were applied during the analytical procedure. Elements were acquired using the following spectrometer crystal configuration: EDS for Ca, W; LiFL for Zn, PETL for Sr, Mo, and Pb, and PETJ for U. The counting time was 30 s for Mn, Fe, Mo, Pb, 70 s for Zn, Sr, U, and 90 s for W and Ca. Natural minerals and synthetic oxides were used for calibration. The results were corrected using ZAF procedures. The detection limit is 0.01% for most elements, but 0.025% for Sr, Mo, and U. The precision for all analyzed elements was better than 1.5%.

In situ LA-ICP-MS trace elements analysis

In situ LA-ICP-MS analysis of scheelite was conducted at the Centre for Ore Deposit and Earth Sciences (CODES), UTAS. An Agilent 7700 ICPMS was equipped with a Coherent Scientific 193 nm Ar-F excimer gas laser and a Resonetics S155 ablation cell. The elements analyzed were ^{23}Na, ^{55}Mn, ^{75}As, ^{88}Sr, ^{89}Y, ^{93}Nb, ^{95}Mo, ^{137}Ba, ^{139}La, ^{140}Ce, ^{141}Pr, ^{146}Nd, ^{147}Sm, ^{153}Eu, ^{157}Gd, ^{159}Tb, ^{163}Dy, ^{165}Ho, ^{166}Er, ^{169}Tm, ^{172}Yb, ^{175}Lu, ^{181}Ta, ^{232}Th, and ^{238}U. Ablation was done in a He atmosphere (0.35 L/min) and immediately mixed with Ar (1.05 L/min) after the ablation cell. The carrier and make-up gas flows were optimized by ablating NIST SRM 612 to obtain maximum sensitivity with ThO/Th <0.2%, U/Th~1.05 and Ca^{2+}/Ca^{+}~0.10. All analyses were made using 29 μm diameter spots, 5 Hz laser repetition rate, on-sample 2.6 J/cm^2 fluence and a 60 s ablation time. Each ablation was preceded by acquisition of a 30 second gas blank, which is subtracted from the signal when the laser is firing. A pre-ablation of 5 laser pulses was performed before analysis and there was a 20 second washout time between analyses. The NIST 610 was used as the primary external standard and average CaO contents of scheelite were used as internal standard assuming stoichiometric Ca in scheelite of 13.9 %. External reproducibility was measured on the secondary standard GSD-1G, with precision for most elements < 5% relative standard deviation (RSD), with the exception of Mo (7.91% RSD; See Supplementary Table 1).

Imaging of trace element distribution in scheelite was conducted using an ASI Resolution S155 laser ablation system equipped with a Coherent COMPex Pro 110 Ar-F excimer gas laser operating at 193 nm and ~20 ns pulse width. The laser ablation system was coupled to an Agilent 7900 ICPMS. The elements analyzed included ^{55}Mn, ^{57}Fe, ^{75}As, ^{88}Sr, ^{89}Y, ^{93}Nb, ^{95}Mo, ^{137}Ba, ^{139}La, ^{140}Ce, ^{141}Pr, ^{146}Nd, ^{147}Sm, ^{153}Eu, ^{157}Gd, ^{159}Tb, ^{163}Dy, ^{165}Ho, ^{166}Er, ^{169}Tm, ^{172}Yb, ^{175}Lu, and ^{238}U. Ablation was done in a He

atmosphere (0.35 L/min) with Ar as the carrier gas (1.05 L/min). Depending on the size of scheelite grains analyzed, the beam size varied from 7 to 11 μm. Spacing between the ablation lines was the same as the laser beam diameter. Laser lines were ablated using a repetition rate of 10 Hz, with laser beam energy at the sample interface maintained at approximately 2.43 J/cm^2. NIST 610 and GSD–1G standards were analyzed before and after each image to assess the drift. Image data was processed following the protocols described in Large et al. (2009).

In situ LA-ICP-MS U-Pb dating

Zircon crystals were separated by conventional heavy-liquid and magnetic methods, and then picked by hand under a binocular microscope. About 150–200 grains were mounted in epoxy and then polished to expose the interior of the crystal. Combined with optical photomicrographs, CL imaging was used to reveal internal structures and aid in selecting targets for U-Pb dating. Zircon U-Pb isotopic dating was carried out at the State Key Laboratory of Geological Processes and Mineral Resources at China University of Geosciences (CUG), Wuhan using a GeoLas2005 laser ablation system equipped with a 193 nm ArF excimer laser, connected to an Agilent 7500a ICP-MS. Analyses were carried out with a beam diameter of 32 μm, frequency of 5Hz and energy of 10 J/cm^2. The instrument settings, analytical procedures and data reduction methods were described in detail in Liu et al. (2008, 2010). Zircon 91500 (Wiedenbeck et al. 1995) was used as the external standard for U-Pb dating, with GJ-1 (Liu et al. 2010) analyzed as a secondary standard. GJ-1 yielded a weighted mean age of 598.3 ± 4.2 Ma (MSWD = 1.4, N=16), which is equivalent to the recommended age within uncertainty (599.6 ± 2.9 Ma, Liu et al. 2010). Data reduction was performed with ICPMSDatacal (Liu et al. 2010) and weighted mean calculations and Concordia diagrams were

produced using ISOPLOT 3.0 (Ludwig 2003).

Apatite U-Pb dating was carried out at CODES, University of Tasmania, using an ASI Resolution S155 laser ablation system equipped with a Coherent COMPex Pro 110 Ar-F excimer gas laser operating at 193 nm and ~20 ns pulse width. The laser ablation system was coupled to an Agilent 7900 ICPMS. The analytical protocols followed those described by Huang et al. (2015) and Thompson et al. (2016). Apatite grains were analyzed in polished rock chips mounted in 25 mm diameter epoxy rounds. Before analysis, transmission, reflection, BSE images and CL images were used to check for inclusions, cracks, and zoning. Apatite was ablated in a He atmosphere (0.35 l/min) using a 29 μm laser spot, 5 Hz repetition rate and an on-sample laser fluence of ~3 J/cm^2. Following a 30 s gas blank, samples were ablated for 30 s. The isotopes measured were ^{31}P, ^{43}Ca, ^{202}Hg, ^{204}Pb, ^{206}Pb, ^{207}Pb, ^{208}Pb, ^{232}Th, and ^{238}U. The reference apatite OD306 (Thompson et al. 2016) was used as a primary standard for the ^{206}Pb/^{238}U ratio with a common Pb correction applied in a similar manner to Chew et al. (2014). The analyses were further verified using secondary apatite standards 401 (Thompson et al. 2016), McClure Mountain (Schoene and Bowring 2006), Otter Lake (Chew et al. 2011), and Emerald Lake (Coulson et al. 2002); the ^{207}Pb-corrected ^{206}Pb/^{238}U ages obtained for these crystals were well within error of published reference ages (See Supplementary Table 2). Trace element concentrations were obtained using NIST 610 as an external calibration standard and ^{43}Ca as an internal standard isotope assuming stoichiometric abundance in apatite (39.4wt.% Ca).

RESULTS

Ore paragenesis and petrography of scheelite

Based on microscopic observation and XRF mapping, the following stages of mineralization were recognized in stratabound Cu-S-rich orebodies in the northern part of the Dabaoshan deposit (Fig. 6).

(1) *Early-stage mineralization*: Ores in this stage are composed chiefly of pyrrhotite and pyrite aggregates (>80%), with grain sizes varying from <50 μm to 5 mm. Based on chemical composition and grain morphology, two types of pyrite (Py1, Py2) can be identified (Figs. 4a and 4d). Py1 occurs as euhedral grains with variable sizes (0.2–5mm). XRF mapping shows that Py1 has marked arsenic zoning (Figs. 4b–4c). Py2 is homogeneous on XRF images, and commonly occurs as fine-grained aggregates (50–100 μm) (Fig. 4e) or overgrowths on Py1 (Fig. 4b).

(2) *Cu-(W) mineralization stage*: Copper mineralization, occurring as chalcopyrite, dominates in this stage. Notably, chalcopyrite replaces the preexisting pyrite along fractures, with evidence for dissolution of the As-rich zones of Py1 (Fig. 4b). Apatite and bismuthinite are sparse and intergrown with chalcopyrite and scheelite (Figs. 5d, 5e). Scheelite mineralization in this stage can be further divided into early- and late-stage. Scheelite in the early-stage (named SchA) occurs as anhedral grains (0.1–0.4 mm). It is embedded in chalcopyrite and disseminated in massive sulfide ores (Fig. 4b). SchA exhibits several distinct features: (1) numerous inclusions, including chalcopyrite, pyrite, ferberite, arsenopyrite, and uraninite (Figs. 5f–5i); (2) chaotic CL texture as demonstrated by the inhomogeneous altitude of brightness (Figs. 7a–7b). In particular, SchA with abundant mineral inclusions exhibits “sieve” textures in CL images (Fig. 7b).

Scheelite in the late-stage (named SchB) occurs as anhedral to subhedral grains in veins crosscutting the massive sulfide ores. These veins contain quartz, calcite, and scheelite, with thickness varying from <1 mm to 5 mm (Fig. 3d). Ferberite is the main inclusion present in SchB (Fig. 5k). Under CL, SchB exhibits a complex texture of coalescing patches with different brightness (Figs. 7c–7d). Based on the contrasting brightness, these patches were subdivided into SchB1 and SchB2. SchB1 is irregular and CL-dark. Some SchB1 patches show oscillatory zonation under CL (Figs. 7d). However, SchB2 comprises CL-bright patches and has a relative homogeneous internal texture (Figs. 7c–7d).

(3) *Late-stage mineralization:* Phlogopite, calcite, talc, and fluorite developed in this stage. Phlogopite occurs as aggregates and replaces the massive sulfide ores (Fig. 4c). Note that original large chalcopyrite is divided into small pieces by phlogopite (Fig. 5l). Locally, massive pyrite-chalcopyrite ores in the form of breccias are cemented by phlogopite, calcite, fluorite, talc, and quartz (Fig. 3e). In addition, calcite-bearing veins are locally observed to crosscut the massive sulfide ores (Fig. 3f).

Chemical characteristics of scheelite

Major element contents are given in Table 1. The complete dataset of trace element composition is listed in Supplementary Table 3 and summarized in Table 2. All types of scheelite in this study showed similar major elements composition with WO_3 varying from 80.3 to 80.25 wt %, and CaO ranging between 19.34 and 19.52 wt % (Table 1). However, SchA and SchB are significantly different in trace element composition.

Both spot analyses (Fig. 8a) and chemical mapping (Fig. 9) corroborated the observation that SchA contained a high density of inclusions. Careful inspection of the time resolved LA-ICP-MS spectra for spot analyses showed that Th and U signals

coincided, occurring mainly as sharp spikes (Fig. 8a). In addition, more than 50% percent of analyses showed short duration spikes in the As signal (Fig. 8a), indicating intersection of the ablation with As-bearing inclusion. Chemical mapping revealed that some tiny REE-bearing inclusions (<10μm), such as monazite and xenotime, are sparsely present in SchA (Fig. 9). Spot analyses with mineral inclusions have been labelled in Supplementary Table 3 and the corresponding elements are not used in the figures. Chemically, SchA contains relatively higher concentrations of most elements, including Na, As, Y, Nb, Mo, Ba, Ta, and rare earth elements (REE), relative to SchB (Table 2). The REE patterns of SchA are uniformly middle REE (MREE)-enriched [$(La/Sm)_N$=0.11–0.46], with negative Eu anomalies (δEu=0.39–0.76) ($\delta Eu=2Eu_N/(Sm_N+Gd_N)$) (Fig. 10a).

In contrast to SchA, the flat time-solved analytical signals for SchB indicate that most trace elements are hosted within the scheelite structure, although U signal spikes are occasionally observed. Spot analyses revealed that SchB1 and SchB2 have similar trace elements compositions, with the exception of U, which is significantly enriched in SchB1 (mean=552 ppm) over SchB2 (mean=2.5 ppm) (Table 2). In addition, Sr concentrations in SchB are slightly higher (mean=147 ppm) than those of SchA (mean=112 ppm). On chondrite-normalized diagrams, SchB1 exhibits various REE patterns (Fig. 10b), with $(La/Sm)_N$ ranging from 0.14 to 10.40, and Eu anomalies varying from 0.72 to 2.74. In contrast, SchB2 shows MREE-enriched patterns with Eu anomalies varying between 0.51 and 1.74 (Fig. 10c). Although SchB2 is relative homogeneous under CL, LA-ICP-MS mapping revealed that it comprises domains with various contents of Sr and REE (Fig. 11).

U-Pb geochronology

The results for zircon and hydrothermal apatite U-Pb dating are given in Supplementary Table 4 and 5, respectively. One scheelite-bearing vein (7902-842) was used for apatite U-Pb dating. Scheelite in this sample belongs to the Sch3-type and a detailed description of this sample has been presented in Su et al. (2019a). Apatite grains from sample 7902-842 are euhedral to subhedral (200–500 μm) and are intergrown with scheelite and chalcopyrite (Figs. 12a-12b). Microscopic observation reveals that scheelite and chalcopyrite crosscut apatite along fractures, but that some apatite grains also contain minor chalcopyrite inclusions (Figs. 12a-12b), indicating that apatite was deposited at the same time as chalcopyrite and scheelite. Apatite is homogenous in BSE images and shows faint zonation in CL images. Most apatite grains contain a relatively higher concentration of U (20–1,029ppm), and lower concentration of Th (<6 ppm), with extremely high U/Th ratios (6.44–16,432.88, median=140) (Supplementary Table 5). The analyses display a wide range of $^{238}U/^{206}Pb$ and $^{207}Pb/^{206}Pb$ ratios. All data plotted on discordia on the Tera-Wasserburg diagram intersecting the concordia curve at 160.8 ± 1.1/1.2 Ma (MSWD = 1.15, n = 29) and the $^{207}Pb/^{206}Pb$ axis at 0.845 ± 0.012 (Fig. 12c), which, within uncertainty, is in line with a terrestrial $^{207}Pb/^{206}Pb$ ratio (0.846) at 160.8 Ma as estimated by the model of Stacey and Kramers (1975). The ^{207}Pb-corrected weighted mean $^{206}Pb/^{238}U$ age was 160.8 ± 0.8 Ma (2σ, MSWD = 0.93, n = 29), consistent with the lower intercept age (Fig. 12d).

Zircons from the Dabaoshan granite porphyry are transparent and light brown. Most zircons display oscillatory zoning under CL, and have Th/U ratios ranging from 0.17 to 0.7, indicating a magmatic origin. Seventeen analyses yielded a weighted mean $^{206}Pb/^{238}U$ age of 161.8 ± 1.0/1.0 Ma (2σ, random errors/systematic errors; MSWD=0.25, n=17) (Figs. 12e–12f).

DISSCUSSION

Age of tungsten-copper mineralization in the footwall

At Dabaoshan, the stratabound orebodies and footwall veinlets comprise a dual structure (Fig. 3a), which is typical for sedimentary exhalative (SEDEX) and/or volcanogenic massive sulfide (VMS) deposits. This feature was used to support the Late Paleozoic SEDEX/VMS model (Ge and Han 1986). However, based on quartz CL textures, trace element signatures, and fluid inclusion studies, Mao et al. (2017) proposed that these veins are genetically associated with the Jurassic porphyry system.

Radioisotopic dating is a powerful tool for understanding the genesis of mineral deposits. Scheelite is generally intergrown with apatite in hydrothermal deposits (e.g., Raimbault et al. 1993; Brugger et al. 2000; Li et al. 2018b; Wu et al. 2019). At Dabaoshan, scheelite is intergrown with chalcopyrite and apatite in the footwall veins (Figs. 12a–12b), indicating a hydrothermal origin. Considering that apatite is a reliable U-Pb geochronometer (e.g., Chew et al. 2011; Huang et al. 2015; Thompson et al. 2016), we propose that apatite U-Pb dating can be used to constrain the formation age of the footwall veins. The LA-ICP-MS zircon U-Pb data suggest that the Dabaoshan granite porphyry crystallized at 161.8 ± 1.0 Ma, which agrees well with previous geochronological studies (Mao et al. 2013b; Li et al. 2012). Hydrothermal apatite dating indicates that scheelite-chalcopyrite veins in the footwall formed at 160.8 ± 1.1 Ma. These two ages are in agreement within uncertainty, corroborating that W-Cu mineralization in the footwall is genetically associated with the Jurassic porphyry Mo-W system.

Formation of scheelite in the stratabound orebodies

Substitution of trace elements into scheelite. Scheelite is characterized by a tetragonal symmetric structure with an irregular dodecahedral $[CaO_8]^{14-}$ group and a tetrahedral $[WO_4]^{2-}$ group, and can incorporate many trace elements (Nassau and Loiacona, 1963; Ghaderi et al. 1999). Divalent cations, such as $^{[VIII]}Fe^{2+}$, $^{[VIII]}Mn^{2+}$, $^{[VIII]}Sr^{2+}$, and $^{[VIII]}Ba^{2+}$, are incorporated into scheelite by substitution for $^{[VIII]}Ca^{2+}$ (Ghaderi et al. 1999). Trivalent elements, such as $^{[VIII]}REE^{3+}$, can be incorporated into the $^{[VIII]}Ca^{2+}$ site via the following substitution mechanisms (Nassau and Loiacona, 1963; Klein and Hurlbut, 1993): (1) $2^{[VIII]}Ca^{2+} = {}^{[VIII]}REE^{3+} + {}^{[VIII]}Na^{+}$ (M1); (2) $^{[VIII]}Ca^{2+} + {}^{[IV]}W^{6+} = {}^{[VIII]}REE^{3+} + {}^{[IV]}Nb^{5+}$ (M2); (3) $3^{[VIII]}Ca^{2+} = 2^{[VIII]}REE^{3+} + \square_{Ca}$ (site vacancy) (M3). Notably, different substitution mechanism exerts a decisive control on REE fractionation between scheelite and ore-forming fluids (Ghaderi et al. 1999; Song et al. 2014; Zhao et al. 2018). Scheelite controlled by vector M1 would preferentially incorporate MREE, while scheelite controlled by vector M3 could inherit the REE patterns of ore-forming fluids (Ghaderi et al. 1999; Brugger et al. 2000; Song et al. 2014). Pentavalent cations, like $^{[IV]}Nb^{5+}$, $^{[IV]}Ta^{5+}$, $^{[IV]}V^{5+}$, and $^{[IV]}As^{5+}$, tend to be incorporated into scheelite via a substitution for $^{[IV]}W^{6+}$ (Nassau and Loiacona, 1963; Dostal et al. 2009; Poulin et al. 2018). Hexavalent cations, such as $^{[IV]}Mo^{6+}$ and $^{[IV]}U^{6+}$, can be incorporated into scheelite by substitution for $^{[IV]}W^{6+}$ (Klein and Hurlbut, 1993; Su et al., 2019b).

Source and nature of ore-forming fluids. Scheelite can record the source and evolution of ore-forming fluids (e.g., Brugger et al. 2000; Song et al. 2014; Liu et al. 2019). At Dabaoshan, scheelite collected from stratabound orebodies shares some common trace element characteristics with scheelite formed in the porphyry system. Previous studies suggest that Y and Ho show similar geochemical behavior due to their

similar ionic radii and ionic charge (Bau and Dulski 1995), and that Y/Ho ratios remain relatively stable during geological processes (i.e. from igneous rocks to clastic sediments; Bau 1996). However, in hydrothermal deposits, the Y/Ho ratio in scheelite can be affected by various factors, such as fluid mixing (Liu et al. 2019) or garnet precipitation (Ding et al. 2018). At Dabaoshan, SchA and SchB showed similar Y/Ho ratios to scheelite in the porphyry systems, as well as the granite porphyry (Fig. 13a), indicating an intimate genetic relationship between tungsten mineralization and the granite porphyry. In addition, the positive correlation between Na atoms and REE + Y – Eu atoms (Fig. 13b) suggests that REE were mainly incorporated into SchA and SchB by the substitution mechanism $REE^{3+} + Na^{+} = 2Ca^{2+}$. This mechanism dominates in scheelite from the Dabaoshan porphyry system (Su et al. 2019a). Furthermore, according to Su et al. (2019a), three generations of scheelite (Sch1–Sch3) were identified at the Dabaoshan porphyry Mo-W deposit (Table 3). From early to late generations, scheelite is gradually depleted in Mo, Nb, Ta, and V, but enriched in U and Th (Figs. 13c–13d) (Su et al. 2019a). Scheelite collected from the stratabound orebodies has a similar trace element composition as the Sch3 in the porphyry system. For example, both SchA and SchB plot mainly in the range of Sch3 (Fig. 13c) on a Mo vs. Nb+Ta diagram, and SchB shows similar U and Th concentrations to Sch3 on the U vs. Th diagram (Fig. 13d). Abundant uraninite inclusions in SchA suggests that SchA also precipitated from fluids enriched in U. Taken together, we infer that fluids responsible for scheelite in the stratabound orebodies were derived from the porphyry systems and were enriched in U and Th.

Precipitation mechanisms for scheelite in stratabound orebodies. The irregular shape, chaotic CL textures, inhomogeneous trace element distribution, and abundant minerals inclusions in SchA suggest that it precipitated from ore-forming fluids under

unstable physiochemical conditions, which may have resulted from phase separation (e.g., Peterson and Mavrogenes 2014), or the interaction between ore-forming fluids and preexisting sulfide minerals and/or the host strata (e.g., Li et al. 2016). At Dabaoshan, fluid-rock interaction is favored over phase separation in the stratabound orebody as a factor facilitating scheelite precipitation because phase separation rarely occurred in the Dabaoshan hydrothermal system (Mao et al. 2017). In addition, fluid-rock interaction is supported by several other lines of evidence. For example, SchA is enriched in Ba (0.19–8.10, mean=3.86 ppm) compared with the scheelite in the porphyry system (mainly <1 ppm) (Su et al. 2019a). The Lower Qiziqiao Formation comprises dolomitic limestone, which generally presents a rich source of Ba (Chakhmouradian et al., 2016 and references there-in). Thus, it is reasonable to infer that ore-forming fluids that significantly interacted with the lower Qiziqiao Formation, liberated Ba from the host rock. In addition, Sch3 in the footwall veins lacks mineral inclusion (Su et al. 2019a), whereas SchA contains arsenopyrite and ferberite inclusions. This indicates that ore-forming fluids responsible for SchA were enriched in As and Fe during Cu-(W) mineralization. XRF mapping results suggest that arsenic-rich Py2 was replaced and dissolved during Cu-(W) mineralization stage (Fig. 4d). Decomposition of arsenic-rich pyrite can release As and Fe into ore-forming fluids (Goldmann et al. 2013), resulting the enrichment of these elements in the fluids.

Uranium commonly substitutes in the fourfold-coordinated $^{[IV]}W^{6+}$ site in scheelite at the Dabaoshan porphyry Mo-W deposit (Su et al. 2019a). However, numerous uraninite inclusions were identified in SchA, indicating great variation in physiochemical conditions (e.g., pH, fO_2, temperature, pressure) during Cu-(W) mineralization stage. Considering the Lower Qiziqiao Formation contains carbonaceous mudstones and massive sulfides, which would act as robust reducing

barriers for U-bearing fluids (Li et al. 2016), fluid-rock interaction would have resulted in a decrease in fO_2. This hypothesis is supported by the occurrence of CH_4-bearing fluid inclusions in quartz coexisting with SchA (our unpublished data). Under reduced conditions, U would be reduced to U^{4+}, which is less soluble in fluids (Langmuir 1978; Bali et al. 2011) and cannot substitute into the scheelite crystal lattice (Su et al. 2019a). Arsenic exists as As^{3+} and/or As^{2-} in fluids, which are not readily incorporated into scheelite structure (Poulin et al. 2018). This explains why so many tiny uraninite and arsenopyrite inclusions occur in SchA (Fig. 5i).

SchB occurs in veins crosscutting the massive sulfide ores, suggesting that it was formed later than the massive sulfide ore. Similar to Sch3 in the footwall veins, SchB1 shows oscillatory zoning in CL images and REE patterns varying from MREE-enriched with a slightly negative Eu anomalies to MREE-depleted with an increasing positive Eu anomaly (Fig. 10b). Scheelite with such feature is generally interpreted to result from fractional crystallization in veins with a limited fluid reserve (e.g., Brugger et al. 2000; Li et al. 2018b; Liu et al. 2019; Su et al. 2019a). It is noteworthy that SchA is more depleted in LREE compared with SchB1(Fig. 10), which reflect co-precipitation of apatite. Apatite is more enriched in LREE relative to HREE than scheelite (Raimbault et al. 1993; Brugger et al. 2000). The precipitation of apatite can fractionate LREE from ore-forming fluids and result in depletion of LREE in scheelite (Raimbault et al. 1993). SchB2 shows relatively constant MREE-enriched patterns and a lack of oscillatory zoning CL textures, which may result from quick precipitation (Brugger et al. 2000). Compared to SchB1, SchB2 is relative CL-bright and depleted in U. This is reflected in the negative correlation between CL intensity and U concentration in scheelite (Su et al. 2019a). All these signatures indicate that SchB resulted from multi-batches of fluid with different chemical composition. Compared with SchA, SchB

contains lower concentrations of Ba (Table 2) and is relatively poor in mineral inclusions (e.g., uraninite, arsenopyrite), indicating limited fluid-rock interaction in veins. Taken together, the evidence suggests that SchB was formed from multiple batches of ore-forming fluid with varying composition, injected intermittently into veins crosscutting the massive sulfide ores.

Implications for the formation of stratabound Cu-Zn-Pb mineralization

In this context, several lines of evidence, including the new dating results and trace elemental characteristics of scheelite in stratabound orebodies, suggest that tungsten mineralization in the stratabound mineralization is genetically associated with the granite porphyry. At Dabaoshan, ore-forming fluids are gradually depleted in Mo, Nb, Ta, and V, but enriched in U and Th during the ore-forming processes (Su et al. 2019a). When fluid emanating from the deep porphyry system encountered the overlying stratabound orebodies and relatively impermeable Qiziqiao Formation, replacement reactions took place and resulted in dramatic variations in physiochemical conditions (e.g. decrease in fO_2, but increase in Ca/Fe, As, Ba). These changes triggered the discharge of fluids, forming scheelite with abundant inclusions and chaotic CL textures. In addition, fluids repeatedly injected into fractures crosscutting the preexisting massive sulfide ores, formed scheelite characterized by patchy CL textures. At Dabaoshan, chalcopyrite coexists with scheelite, not only in the footwall, but also in the stratabound orebodies. It is noteworthy that Cu and W concentrations co-vary in drill cores from deep to shallow levels (Fig. 14), indicating that Cu, at least locally, was derived from the same source as W at Dabaoshan. This view is further supported by the following evidence: (1) fluid inclusion in porphyry-related veins contain an average concentration of 0.04 g/L Cu, 0.2 g/L Pb, and 0.1 g/L Zn (Cai and Liu 1993); (2) The

porphyry system and stratabound orebodies have similar quartz CL textures, trace element, and H-O-S isotopic characteristics, indicating that the Jurassic porphyry system contributed significantly to the stratabound base mental mineralization (Mao et al. 2017).

Based on the replacement textures and crosscutting relationships, it can be confirmed that pyrite and pyrrhotite formed earlier than Cu-W mineralization in the stratabound orebodies. However, we cannot preclude the possibility that pyrite and pyrrhotite were formed during a previous mineralization event. It is noteworthy that Ying et al. (2017) reported a pyrrhotite Re-Os age of 410±16 Ma (N=6, MSWD=15) for the stratabound orebodies, indicating a late Devonian mineralization event. Additional work is still required to temporally constrain the formation of stratabound orebodies at Dabaoshan.

IMPLICATIONS

A combination of scheelite trace element signatures, CL textures, and apatite U-Pb dating provide new insights into the ore genesis and W mineralization at the Dabaoshan stratabound polymetallic deposit, as follows.

(1) Scheelite-chalcopyrite veins in the footwall of stratabound orebodies formed at 160.8 ± 1.1 Ma. This age agrees well with crystallization age of the Dabaoshan granite porphyry (161.8 ± 1.0 Ma), indicating a close genetic relationship between footwall mineralization and the Dabaoshan granite porphyry.

(2) Scheelites in stratabound orebodies and porphyry systems share similar trace elemental characteristics, demonstrating that ore-forming fluids responsible for scheelite formation in stratabound orebodies were derived from the Dabaoshan porphyry system.

(3) Ore-forming fluids interacted with the overlying Lower Qiziqiao Formation and stratabound orebodies, resulting in SchA, characterized by numerous minerals inclusions, chaotic CL textures and enrichment in Ba. Multiple batches of fluid penetrated the stratabound orebodies along fractures, resulting in SchB, characterized by coalescing patches with different CL textures.

(4) Scheelite chemistry can be a powerful tool to decipher the genetic relationship between porphyry system and the adjacent stratabound mineralization.

ACKNOWLEDGEMENTS

This research was financially supported by China Geological Survey (No. 12120115035401), National Natural Science Foundation of China (No. 42073040), China Geological Survey (No. 12120114067101), and the Student Research Grant (SGR-17-37) for Society of Economic Geologists. We thank Karsten Goemann and Sandrin Feig from the Central Science Laboratory, University of Tasmania, for assisting with microprobe and BSE analyses.

REFERENCES

Bali, E., Keppler, H., and Audetat, A. (2012) The mobility of W and Mo in subduction zone fluids and the Mo–W–Th–U systematics of island arc magmas. Earth and Planetary Science Letters, 351-352, 195-207.

Bau, M. (1996) Controls on the fractionation of isovalent trace elements in magmatic and aqueous systems: evidence from Y/Ho, Zr/Hf, and lanthanide tetrad effect. Contributions to Mineralogy and Petrology, 123(3), 323-333.

Bau, M., and Dulski, P. (1995) Comparative study of yttrium and rare-earth element behaviours in fluorine-rich hydrothermal fluids. Contributions to Mineralogy and Petrology, 119(2-3), 213-223.

Bonnetti, C., Liu, X., Mercadier, J., Cuney, M., Deloule, E., Villeneuve, J., and Liu, W. (2018) The genesis of granite-related hydrothermal uranium deposits in the Xiazhuang and Zhuguang ore fields, North Guangdong Province, SE China: Insights from mineralogical, trace elements and U-Pb isotopes signatures of the U mineralisation. Ore Geology Reviews, 92, 588-612.

Brugger, J., Lahaye, Y., Costa, S., Lambert, D., and Bateman, R. (2000) Inhomogeneous distribution of REE in scheelite and dynamics of Archaean hydrothermal systems (Mt. Charlotte and Drysdale gold deposits, Western Australia). Contributions to Mineralogy and Petrology, 139(3), 251-264.

Cai, J., and Liu, J. (1993) Research and its application on the inclusions characteristics in the Dabaoshan polymetallic deposit, Northern Guangdong. Journal of Mineralogy and Petrology, 1, 33-40 (in Chinese with English abstract).

Cao, Y., Gao, F., Du, Y., Du, Y., and Pang, Z. (2016) Genesis of the Datuanshan stratabound skarn Cu(–Mo) deposit, Middle–Lower Yangtze Valley, Eastern China: constraints from geology, Re–Os geochronology, mineralogy, and sulfur isotopes. Mineralium Deposita, 1-20.

Chakhmouradian, A.R., Reguir, E.P., Cou slan, C., and Yang, P. (2016) Calcite and dolomite in intrusive carbonatites. II. Trace-element variations. Mineralogy and Petrology, 110(2-3), 361-377.

Charvet, J., Shu, L.S., Shi, Y.S., Guo, L.Z., and Faure, M. (1996) The building of south China: collision of Yangzi and Cathaysia blocks, problems and tentative answers. Journal of Southeast Asian Earth Sciences, 13(3), 223-235.

Chew, D.M., Petrus, J.A., and Kamber, B.S. (2014) U–Pb LA–ICPMS dating using accessory mineral standards with variable common Pb. Chemical Geology, 363, 185-199.

Chew, D.M., Sylvester, P.J., and Tubrett, M.N. (2011) U–Pb and Th–Pb dating of apatite by LA-ICPMS. Chemical Geology, 280(1), 200-216.

Coulson, I.M., Villeneuve, M.E., Dipple, G.M., Duncan, R.A., Russell, J.K., and Mortensen, J.K. (2002) Time-scales of assembly and thermal history of a composite felsic pluton: constraints from the Emerald Lake area, northern Canadian Cordillera, Yukon. Journal of Volcanology and Geothermal Research, 114(3), 331-356.

Dai, T., Yin, X., and Zhang, D. (2015) Ore-forming model of Dabaoashan poly-metal deposit in Guangdong Province. Journal of Central South University, 46(7), 2693-2700 (in Chinese with English abstract).

Ding, T., Ma, D., Lu, J., and Zhang, R. (2018) Garnet and scheelite as indicators of multi-stage tungsten mineralization in the Huangshaping deposit, southern Hunan province, China. Ore Geology Reviews, 94, 193-211.

Dostal, J., Kontak, D.J., and Chatterjee, A.K. (2009) Trace element geochemistry of scheelite and rutile from metaturbidite-hosted quartz vein gold deposits, Meguma Terrane, Nova Scotia, Canada: genetic implications. Mineralogy &

Petrology, 97(1), 95-109.

Ge, C.H., and Han, F. (1986) Submarine volcanic hydrothermal sedimentary origin of the Dabaoshan iron and polymetallic deposit. Mineral Deposits, 5, 1-12 (in Chinese with English abstract).

Ghaderi, M., Palin, J.M., Campbell, I.H., and Sylvester, P.J. (1999) Rare earth element systematics in scheelite from hydrothermal gold deposits in the Kalgoorlie-Norseman region, Western Australia. Economic Geology, 94(3), 423-437.

Goldmann, S., Melcher, F., G?bler, H., Dewaele, S., Clercq, F.D., and Muchez, P. (2013) Mineralogy and Trace Element Chemistry of Ferberite/Reinite from Tungsten Deposits in Central Rwanda. Minerals, 3(2), 121-144.

Gu, L.X., Zaw, K., Hu, W.X., Zhang, K.J., Ni, P., He, J.X., Xu, Y.T., Lu, J.J., and Lin, C.M. (2007) Distinctive features of Late Palaeozoic massive sulphide deposits in South China. Ore Geol Rev. Ore Geology Reviews, 31(1-4), 107-138.

Guangdong Geophysics prospecting party, 2015. Research report of the geochemical field of mine clusters and prospecting. p. (In Chinese)

Hsü, K.J., Li, J., Chen, H., Wang, Q., Sun, S., and Şengör, A.M.C. (1990) Tectonics of South China: Key to understanding West Pacific geology. Tectonophysics, 183(1), 9-39.

Hu, R.Z., Bi, X.W., Zhou, M.F., Peng, J.T., Su, W.C., Liu, S., and Qi, H.W. (2008) Uranium Metallogenesis in South China and Its Relationship to Crustal Extension during the Cretaceous to Tertiary. Economic Geology, 103(3), 583-598.

Huang, Q., Kamenetsky, V.S., McPhie, J., Ehrig, K., Meffre, S., Maas, R., Thompson, J., Kamenetsky, M., Chambefort, I., Apukhtina, O., and Hu, Y. (2015) Neoproterozoic (ca. 820–830Ma) mafic dykes at Olympic Dam, South Australia: Links with the Gairdner Large Igneous Province. Precambrian Research, 271, 160-172.

Huang, S., Zeng, Y., Jia, G., and Chen, Y. (1987) On the genesis of Dabaoshan polymetallic deposit in Guangdong Province, China. Chinese Journal of Geochemistry, 6(4), 322-330.

Huang, W.T., Liang, H.Y., Wu, J., Zou, Y.Q., and Zhang, J. (2017) Formation of porphyry Mo deposit in a deep fault zone, example from the Dabaoshan porphyry Mo deposit in northern Guangdong, South China. Ore Geology Reviews, 81, Part 2, 940-952.

Klein, C., and Hurlbut Jr, C.S. (1993) Manual of mineralogy. Manual of Mineralogy. John Wiley and Sons, New York, pp. 681.

Langmuir, D. (1978) Uranium solution-mineral equilibria at low temperatures with applications to sedimentary ore deposits. Geochimica et Cosmochimica Acta, 42(6, Part A), 547-569.

Large, R.R., Danyushevsky, L., Hollit, C., Maslennikov, V., Meffre, S., Gilbert, S., Bull, S., Scott, R., Emsbo, P., and Thomas, H. (2009) Gold and Trace Element Zonation in Pyrite Using a Laser Imaging Technique: Implications for the Timing of Gold in Orogenic and Carlin-Style Sediment-Hosted Deposits. Economic Geology, 104(5), 635-668.

Li, C.Y., Zhang, H., Wang, F.Y., Liu, J.Q., Sun, Y.L., Hao, X.L., Li, Y.L., and Sun, W.D. (2012) The formation of the Dabaoshan porphyry molybdenum deposit induced by slab rollback. Lithos, 150(0), 101-110.

Li, X.-Y., Gao, J.-F., Zhang, R.-Q., Lu, J.-J., Chen, W.-H., and Wu, J.-W. (2018b) Origin of the Muguayuan veinlet-disseminated tungsten deposit, South China: Constraints from in-situ trace element analyses of scheelite. Ore Geology Reviews, 99, 180-194.

Li, Y., Duan, C., Zhao, Y., Pei, H., and Ren, S. (2016) The Role of Oxidizing Reducing Barrier in Mineralization of Hydrothermal Uranium Ore. Acta Geologica Sinica, 90(2), 201-218 (in Chinese with English abstract).

Li, Y., Selby, D., Li, X.-H., and Ottley, C.J. (2018a) Multisourced metals enriched by magmatic-hydrothermal fluids in stratabound deposits of the Middle–Lower Yangtze River metallogenic belt, China. Geology, 46(5), 391-394.

Li, Z.-X., and Li, X.-H. (2007) Formation of the 1300-km-wide intracontinental orogen and postorogenic magmatic province in Mesozoic South China: A flat-slab subduction model. Geology, 35(2), 179-182.

Li, Z.X., Zhang, L.H., and Mca. Powell, C. (1995) South China in Rodinia: Part of the missing link between Australia East Antarctica and Laurentia? Geology, 23(5), 407.

Liu, B., Li, H., Wu, Q.-H., Evans, N.J., Cao, J.-Y., Jiang, J.-B., and Wu, J.-H. (2019) Fluid evolution of Triassic and Jurassic W mineralization in the Xitian ore field, South China: Constraints from scheelite geochemistry and microthermometry.

Lithos, 330-331, 1-15.

Liu, Y.S., Hu, Z.C., Gao, S., Günther, D., Xu, J., Gao, C.G., and Chen, H.H. (2008) In situ analysis of major and trace elements of anhydrous minerals by LA-ICP-MS without applying an internal standard. Chemical Geology, 257(1), 34-43.

Liu, Y.S., Hu, Z.C., Zong, K.Q., Gao, C.G., Gao, S., Xu, J., and Chen, H.H. (2010) Reappraisement and refinement of zircon U-Pb isotope and trace element analyses by LA-ICP-MS. Chinese Science Bulletin, 55(15), 1535-1546.

Ludwig, K.R. (2003) Users manual for Isoplot/Ex: a geochronological toolkit for Microsoft Excel. 1a.

Mao, J., Cheng, Y., Chen, M., and Pirajno, F. (2013a) Major types and time–space distribution of Mesozoic ore deposits in South China and their geodynamic settings. Mineralium Deposita, 48(3), 267-294.

Mao, J., Pirajno, F., and Cook, N. (2011a) Mesozoic metallogeny in East China and corresponding geodynamic settings — An introduction to the special issue. Ore Geology Reviews, 43(1), 1-7.

Mao, J., Xie, G., Duan, C., Pirajno, F., Ishiyama, D., and Chen, Y. (2011b) A tectono-genetic model for porphyry–skarn–stratabound Cu–Au–Mo–Fe and magnetite–apatite deposits along the Middle–Lower Yangtze River Valley, Eastern China. Ore Geology Reviews, 43(1), 294-314.

Mao, W., Li, X.F., and Yang, F.C. (2013b) Zircon LA-ICP-MS U-Pb ages of granites at Dabaoshan polymetallic deposit and its geological significance, Guangdong, South China. Acta Petrologica Sinica, 29(12), 4104-4120 (in Chinese with

English abstract).

Mao, W., Rusk, B., Yang, F., and Zhang, M. (2017) Physical and Chemical Evolution of the Dabaoshan Porphyry Mo Deposit, South China: Insights from Fluid Inclusions, Cathodoluminescence, and Trace Elements in Quartz. Economic Geology, 112(4), 889-918.

Nassau, K., and Loiacono, G. (1963) Calcium tungstate—III: Trivalent rare earth substitution. Journal of Physics and Chemistry of Solids, 24(12), 1503-1510.

Pan, H., Kang, Z., and Cao, Y. (2018) Re-Os isotopic dating age of molybdenite for Chuandu Mo deposit and its geological significance in Dabaoshan ore-field,North Guangdong. Mineral Resources and Geology, 32, 27-38 (in Chinese with English abstract).

Pan, Y., and Dong, P. (1999) The Lower Changjiang (Yangzi/Yangtze River) metallogenic belt, east central China: intrusion- and wall rock-hosted Cu–Fe–Au, Mo, Zn, Pb, Ag deposits. Ore Geology Reviews, 15(4), 177-242.

Peterson, E.C., and Mavrogenes, J.A. (2014) Linking high-grade gold mineralization to earthquake-induced fault-valve processes in the Porgera gold deposit, Papua New Guinea. Geology, 42(5), 383-386.

Pirajno, F., and Zhou, T. (2015) Intracontinental Porphyry and Porphyry-Skarn Mineral Systems in Eastern China: Scrutiny of a Special Case “Made-in-China”. Economic Geology, 110(3), 603-629.

Poulin, R.S., Mcdonald, A.M., Kontak, D.J., and Mcclenaghan, M.B. (2016) On the Relationship Between Cathodoluminescence and the Chemical Composition of

Scheelite From Geologically Diverse Ore-Deposit Environments. Canadian Mineralogist, 54(5), 1147-1173.

Poulin, R.S., Kontak, D.J., Mcdonald, A.M., and Mcclenaghan, M.B. (2018) Assessing Scheelite As an Ore-deposit Discriminator Using Its Trace-element and REE Chemistry. The Canadian Mineralogist, 56(3), 265-302.

Qin, K., Zhai, M., Li, G., Zhao, J., Zeng, Q., Gao, J., Xiao, W., Li, J., and Sun, S. (2017) Links of collage orogenesis of multiblocks and crust evolution to characteristic metallogeneses in China. Acta Petrologica Sinica, 33(2), 305-325 (in Chinese with English abstract).

Raimbault, L., Baumer, A., Dubru, M., Benkerrou, C., Croze, V., and Zahm, A. (1993) REE fractionation between scheelite and apatite in hydrothermal conditions. American Mineralogist, 78(11), 1275-1285.

Schoene, B., and Bowring, S.A. (2006) U–Pb systematics of the McClure Mountain syenite: thermochronological constraints on the age of the 40 Ar/ 39 Ar standard MMhb. Contributions to Mineralogy & Petrology, 151(5), 615-630.

Song, G., Qin, K., Li, G., Evans, N.J., and Chen, L. (2014) Scheelite elemental and isotopic signatures:Implications for the genesis of skarn-type W-Mo deposits in the Chizhou Area,Anhui Province,Eastern China. American Mineralogist, 99(2-3), 303-317.

Stacey, J.S., and Kramers, J.D. (1975) Approximation of terrestrial lead isotope evolution by a two-stage model. Earth and Planetary Science Letters, 26(2), 207-221.

Su, S.-Q., Qin, K.-Z., Li, G.-M., Olin, P., and Thompson, J. (2019a) Cathodoluminescence and trace elements of scheelite: Constraints on ore-forming processes of the Dabaoshan porphyry Mo-W deposit, South China. Ore Geology Reviews, 115, 103183.

Su, S., Qin, K., Li, G., Pang, X., Zou, X., and Zhao, C. (2019b) Geochronology and geochemistry of Early Silurian felsic volcanic rocks in the Dabaoshan ore district, South China: Implications for the petrogenesis and geodynamic setting. Geological Journal, 54(6), 3286-3303.

Sun, S.S., and Mcdonough, W.F. (1989) Chemical and isotopic systematics of oceanic basalts: implications for mantle composition and processes. Geological Society London Special Publications, 42(1), 313-345.

Sun, W., Ding, X., Hu, Y.-H., and Li, X.-H. (2007) The golden transformation of the Cretaceous plate subduction in the west Pacific. Earth and Planetary Science Letters, 262(3-4), 533-542.

Thompson, J., Meffre, S., Maas, R., Kamenetsky, V., Kamenetsky, M., Goemann, K., Ehrig, K., and Danyushevsky, L. (2016) Matrix effects in Pb/U measurements during LA-ICP-MS analysis of the mineral apatite. Journal of Analytical Atomic Spectrometry, 31(6), 1206-1215.

Wang, L., Hu, M.G., Yang, Z., Qu, W.J., Xia, J.L., and Chen, K.X. (2011) U–Pb and Re–Os geochronology and geodynamic setting of the Dabaoshan polymetallic deposit, northern Guangdong Province, South China. Ore Geology Reviews, 43(1), 40-49.

Wang, L., Jin, X., Xu, D., Cai, J., and Wang, Y. (2019) Geochronological, geochemical, and Nd–Hf isotopic constraints on the origin of magmatism in the Dabaoshan ore district of South China. Geological Journal, 54, 1518-1534.

Wang, Y.J., Fan, W.M., Zhang, G.W., and Zhang, Y.H. (2013) Phanerozoic tectonics of the South China Block: Key observations and controversies. Gondwana Research, 23(4), 1273-1305.

Wiedenbeck, M., Alle, P., Corfu, F., Griffin, W., Meier, M., Oberli, F.v., Quadt, A.v., Roddick, J., and Spiegel, W. (1995) Three natural zircon standards for U-Th-Pb, Lu-Hf, trace element and REE analyses. Geostandards newsletter, 19(1), 1-23.

Wu, J., Wang, G.Q., Liang, H.Y., Huang, W.T., Lin, S.P., Zou, Y.Q., Sun, W.D., and Wang, Y.W. (2014) Indentification of Caledonian volcanic rock in the Dabaoshan ore-field in northern Guangdong Province and its geological implication. Acta Petrologica Sinica, 30(4), 1145-1154 (in Chinese with English abstract).

Wu, S., Sun, W., and Wang, X. (2019) A new model for porphyry W mineralization in a world-class tungsten metallogenic belt. Ore Geology Reviews, 107, 501-512.

Ying, L., Wang, D., Li, C., Wang, K., Wang, L., Wang, Y., Zhang, X., and Jiang, J. (2017) Re-Os dating of sulfides in the north stratiform ore body in Dabaoshan, Guangdong Province and its indication. Earth Science Frontiers, 24(5), 31-38.

Zaw, K., Peters, S.G., Cromie, P., Burrett, C., and Hou, Z. (2007) Nature, diversity of deposit types and metallogenic relations of South China. Ore Geology Reviews, 31(1), 3-47.

Zhang, Y., Shao, Y.J., Chen, H.Y., Liu, Z.F., and Li, D.F. (2017) A hydrothermal origin for the large Xinqiao Cu-S-Fe deposit, Eastern China: Evidence from sulfide geochemistry and sulfur isotopes. Ore Geology Reviews, 88, 534-549.

Zhao, W.W., Zhou, M.-F., Williams-Jones, A.E., and Zhao, Z. (2018) Constraints on the uptake of REE by scheelite in the Baoshan tungsten skarn deposit, South China. Chemical Geology, 477, 123-136.

Zhou, X., Sun, t., Shen, W., Shu, l., and Niu, Y. (2006) Petrogenesis of Mesozoic granitoids and volcanic rocks in South China: A response to tectonic evolution. Episodes, 29(1), 26-33.

Zhou, X.M., and Li, W.X. (2000) Origin of Late Mesozoic igneous rocks in Southeastern China: implications for lithosphere subduction and underplating of mafic magmas. Tectonophysics, 326(3), 269-287.

CAPTION

FIGURE 1. Geological map of the Dabaoshan ore district in a regional context (a), and of the study area (b). Section AB (detailed in Figure 2) and drill hole locations are shown. Modified after Mao et al. (2017) and Su et al. (2019b).

FIGURE 2. Cross-section AB illustrating the spatial distribution of different types of vein and stratabound orebodies at the Dabaoshan deposit. Also shown are the drillholes with scheelite sample locations. V1 = quartz-molybdenite veins; V2 = quartz-pyrite±scheelite veins; V3 = quartz-pyrite-chalcopyrite-scheelite veins； V4 = quartz-

pyrite-sphalerite-galena veins.

FIGURE 3. Photographs of stratabound orebodies and massive sulfide ores at Dabaoshan. (a) Stratabound orebodies and the footwall stockworks mimic the dual structure of a typical VMS deposit. (b) Numerous pyrite veins with sericite alteration are distributed below stratabound orebodies. (c) Representative massive chalcopyrite-pyrite ore. (d) Representative massive pyrite ore crosscut by calcite-quartz-scheelite veins. (e) Brecciated massive sulfide ore, cemented by phlogopite and clay minerals. (f) Representative massive chalcopyrite-pyrite ore crosscut by calcite veins. Cc = calcite, Ccp = chalcopyrite, Phl = phlogopite, Py = pyrite, Qtz = quartz.

FIGURE 4. Combined synchrotron XRF images of massive sulfide ores. Photographs of samples are shown in Fig. 3c and 3d, respectively. Cc = calcite, Ccp = chalcopyrite, Phl = phlogopite, Py = pyrite, Qtz = quartz.

FIGURE 5. Reflected light images (crossed nicols) and BSE images associated with scheelite in massive sulfide ores. (a) Massive pyrrhotite occurs in the early-stage mineralization. (b) Pyrrhotite is intergrown with pyrite in the early-stage mineralization. (c) SchA and chalcopyrite replaced the preexisting pyrite. (d) Bismuthinite is intergrown with chalcopyrite in the Cu-(W) mineralization stage. (e) Apatite occurs as anhedral grains and is interstitial among pyrite. (f–h) SchA contains numerous

inclusions, including pyrite, chalcopyrite, arsenopyrite, and ferberite. (i) SchA contains tiny uraninite inclusions. (j) Quartz-scheelite veins crosscut massive pyrite ores. (k) SchB contains minor ferberite and pyrite inclusions. (l) Chalcopyrite was replaced by phlogopite. Note that Figs. e, h, and i are BSE images while the rest are reflected light images. Ap = apatite, Apy = arsenopyrite, Bis = bismuthinite, Cc = calcite, Ccp = chalcopyrite, Frt = ferberite, Phl = phlogopite, Po = pyrrhotite, Py = pyrite, Qtz = quartz. Ur = uraninite.

FIGURE 6. Paragenetic sequence of stratabound Cu-S mineralization in Dabaoshan deposit.

FIGURE 7. Representative CL images of scheelite in massive sulfide ores. (a) Representative SchA shows chaotic textures in CL images. (b) SchA with a high density of inclusions shows "sieve" texture on CL image. Reflected light image of the same SchA grain is shown in Fig. 5f. (c) Representative SchB shows a complex texture of coalescing patches with different brightness. Note that SchB1 is CL-dark whereas SchB2 is CL-bright. (d) Representative SchB, in which SchB1 is CL-dark with notable oscillatory zoning. Mineral abbreviations as in Figure 4 and 5.

FIGURE 8. Representative time-resolved signals obtained by depth profile analysis of scheelite in massive sulfide ores at Dabaoshan. (a) Peaks of U and Th in SchA indicate an inclusion of uraninite, and the As peak indicates the existence of an arsenopyrite

inclusion. (b) SchB1 shows a flat, stable signals for all elements during ablation.

FIGURE 9. Photomicrographs and LA-ICP-MS maps of trace element contents in SchA. Scale in counts per second.

FIGURE 10. Chondrite-normalized REE patterns for different types of scheelite from the massive sulfide ores at Dabaoshan. The normalized values for chondrite are from Sun and McDonough (1989).

FIGURE 11. CL image and LA-ICP-MS maps of trace elements in SchB. Scale in counts per second.

FIGURE 12. (a-b) Representative apatite crystal, intergrown with scheelite. (c) The U-Pb Tera-Wasserburg concordia diagram for apatite. (d) The ^{207}Pb-corrected ^{206}Pb/^{238}U weighted mean age for apatite. (e-f) Zircon U-Pb concordant curves and weighted average age of the Dabaoshan granite porphyry. Individual precision ellipses and error bars are plotted at 2σ. Age uncertainties are quoted as 2σ. MSWD = mean square of weighted deviates.

FIGURE 13. (a) Y vs. Ho for scheelite; (b) Plot of Na vs. REE+Y-Eu for SchA and SchB; (c) Mo vs. Nb+Ta for scheelite; (d) U vs. Th for scheelite. Data for granite porphyry and scheelite from Dabaoshan porphyry system are from Huang et al. (2017) and Su et al. (2019a), respectively.

FIGURE 14. Concentrations of W and Cu in ores from drill cores. Revised after Guangdong Geophysics Prospecting Party (2015).

Table 1. Major elements of Scheelite from the Dabaoshan stratabound deposit (%)

Elemant	SchA (n=20)		SchB (n=20)	
	Mean	Range	Mean	Range
CaO	19.34	18.99-19.70	19.52	19.10-20.21
WO_3	80.3	79.34-81.73	80.26	79.16-81.48
MnO	n.d.	n.d.	n.d.	n.d.-0.06
FeO	0.01	n.d.-0.05	0.08	0.01-0.43
ZnO	n.d.	n.d.	n.d.	n.d.-0.01
SrO	0.02	n.d.-0.06	n.d.	n.d.-0.08
MoO_3	n.d.	n.d.-0.03	n.d.	n.d.-0.04
PbO	n.d.	n.d.	n.d.	n.d.
UO_2	0.01	n.d.-0.12	n.d.	n.d.-0.03
Total	99.68	98.66-101.48	99.88	98.86-101.21

Table 2. Trace elements concentrations (ppm) for each type of scheelite in this study

		Na	Mn	As	Sr	Y	Nb	Mo
Average detection limit		1.94	0.19	0.25	0.001	0.001	0.001	0.005
SchA	Median	110	21.6	151	97.5	306	8.46	6.63
n=26	sd	22.8	211	50.4	68.6	68.6	1.99	16.4
	Min	66.3	7.45	37.9	43.7	147	4.35	1.40
	Max	158	617	208	363	458	11.6	68.6
SchB1	Median	52.8	23.4	0.73	156	41.8	0.90	0.29
n=19	sd	75.0	191	2.36	33.5	80.0	0.57	0.23
	Min	23.5	7.99	bdl	86.8	7.32	0.69	bdl
	Max	277	882	9.79	229	294	2.90	0.92
SchB2	Median	45.9	9.77	0.87	114	90.9	1.53	0.34
n=8	sd	9.95	31.8	3.38	54.6	17.2	1.10	0.27
	Min	38.2	2.73	0.45	70.1	59.4	0.64	0.21
	Max	72.2	105	11.0	228	117	4.13	1.02

Ba	REE	Ta	Th	U
0.004	<0.001	0.0006	0.001	0.0006
3.86	905	0.104	0.29	/
1.98	215	0.018	0.20	/
0.19	356	0.088	0.01	/
8.10	1280	0.156	0.67	/
0.37	397	0.010	1.94	420
0.57	297	0.071	1.60	555
0.07	134	0.004	0.07	15.9
1.90	1129	0.303	6.00	1862
0.17	360	0.008	1.09	1.83
0.66	50	0.041	0.75	2.52
0.01	264	0.004	bdl	0.03
2.07	437	0.104	2.23	5.83

Table 3. Summary of different types of scheelite at Dabaoshan

	Scheelite type	Principal mineral assemblage	Host rock
Porphry Mo-W mineralization	Sch1	Qtz-Py-Mo-Sch vein	Granite porphyry
	Sch2	Qtz-Py-Sch vein	Granite prophyry, Silurian dacite, Devonian Lahutou Formation
	Sch3	Qtz-Py-Ccp-Sch-Ap vein	Silurian dacite, Devonian Lahutou Formation Devonian Qiziqiao Formation
Stratbound Cu-S mineralization	SchA	Py-Ccp-Sch	Devonian Qiziqiao Formation
	SchB	Qtz-Sch-Cc veins	Devonian Qiziqiao Formation

Abbreviations: Ap-apatite, Cc-calcite, Ccp-chalcopyrite,Mo-molybdenite, Py-pyrite,Qtz-quartz, Sch-sch

CL characteristic	Reference
CL-dark and homogeneous	
CL-bright	Su et al. 2019a
oscillatory zoning	
chaotic CL texture, containg numerous mineral inclusions comprise patches with different CL brightness	This study

eelit

Figure 1

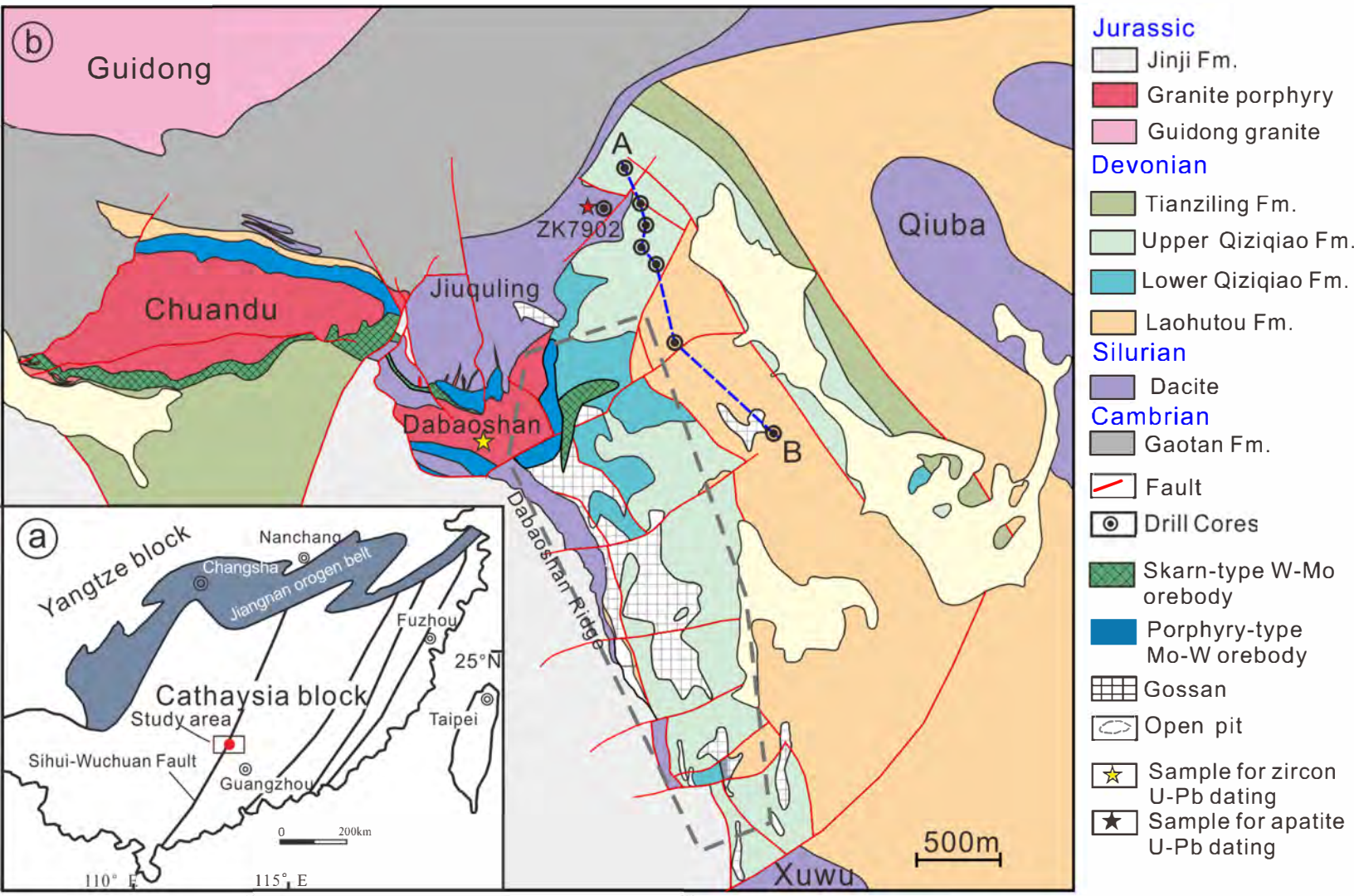
b
Guidong
Chuandu
Jiuquling
Dabaoshan
ZK7902
A
B
Qiuba
Xuwu
Dabaoshan Ridge
500m
a
Yangtze block
Nanchang
Changsha
Jiangnan orogen belt
Fuzhou
25°N
Cathaysia block
Study area
Taipei
Sihui-Wuchuan Fault
Guangzhou
0
200km
110° E
115° E
Jurassic
Jinji Fm.
Granite porphyry
Guidong granite
Devonian
Tianziling Fm.
Upper Qiziqiao Fm.
Lower Qiziqiao Fm.
Laohutou Fm.
Silurian
Dacite
Cambrian
Gaotan Fm.
Fault
Drill Cores
Skarn-type W-Mo orebody
Porphyry-type Mo-W orebody
Gossan
Open pit
Sample for zircon U-Pb dating
Sample for apatite U-Pb dating

Figure 2

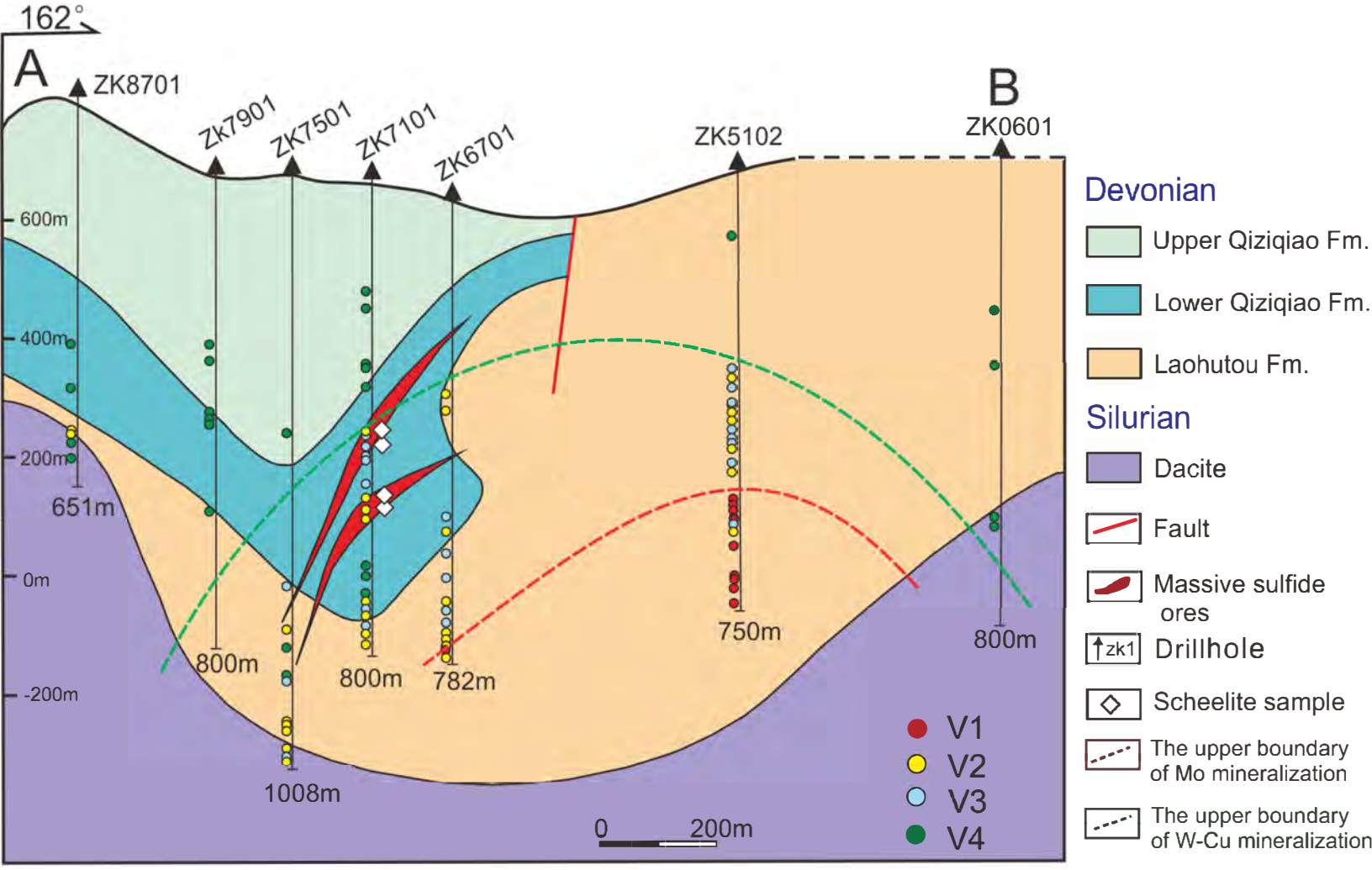
162°
A
B
ZK8701
Zk7901
ZK7501
ZK7101
ZK6701
ZK5102
ZK0601
600m
400m
200m
0m
-200m
651m
800m
800m
782m
1008m
750m
800m
0
200m
V1
V2
V3
V4
Devonian
Upper Qiziqiao Fm.
Lower Qiziqiao Fm.
Laohutou Fm.
Silurian
Dacite
Fault
Massive sulfide ores
zk1
Drillhole
Scheelite sample
The upper boundary of Mo mineralization
The upper boundary of W-Cu mineralization

Figure 3

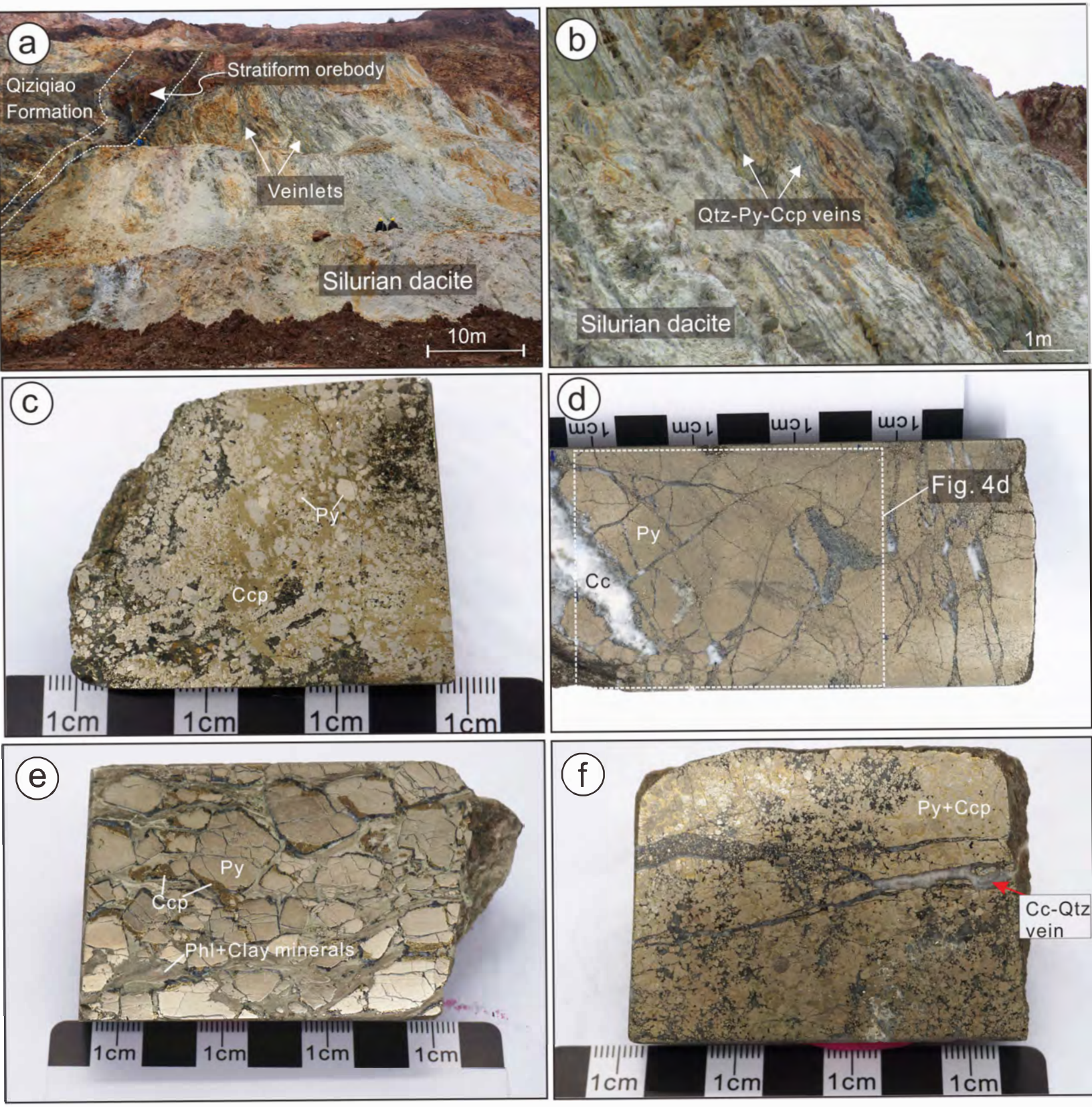
a
Qiziqiao Formation
Stratiform orebody
Veinlets
Silurian dacite
10m
b
Qtz-Py-Ccp veins
Silurian dacite
1m
c
Py
Ccp
1cm
d
Fig. 4d
Py
Cc
e
Py
Ccp
Phl+Clay minerals
f
Py+Ccp
Cc-Qtz vein

Figure 4

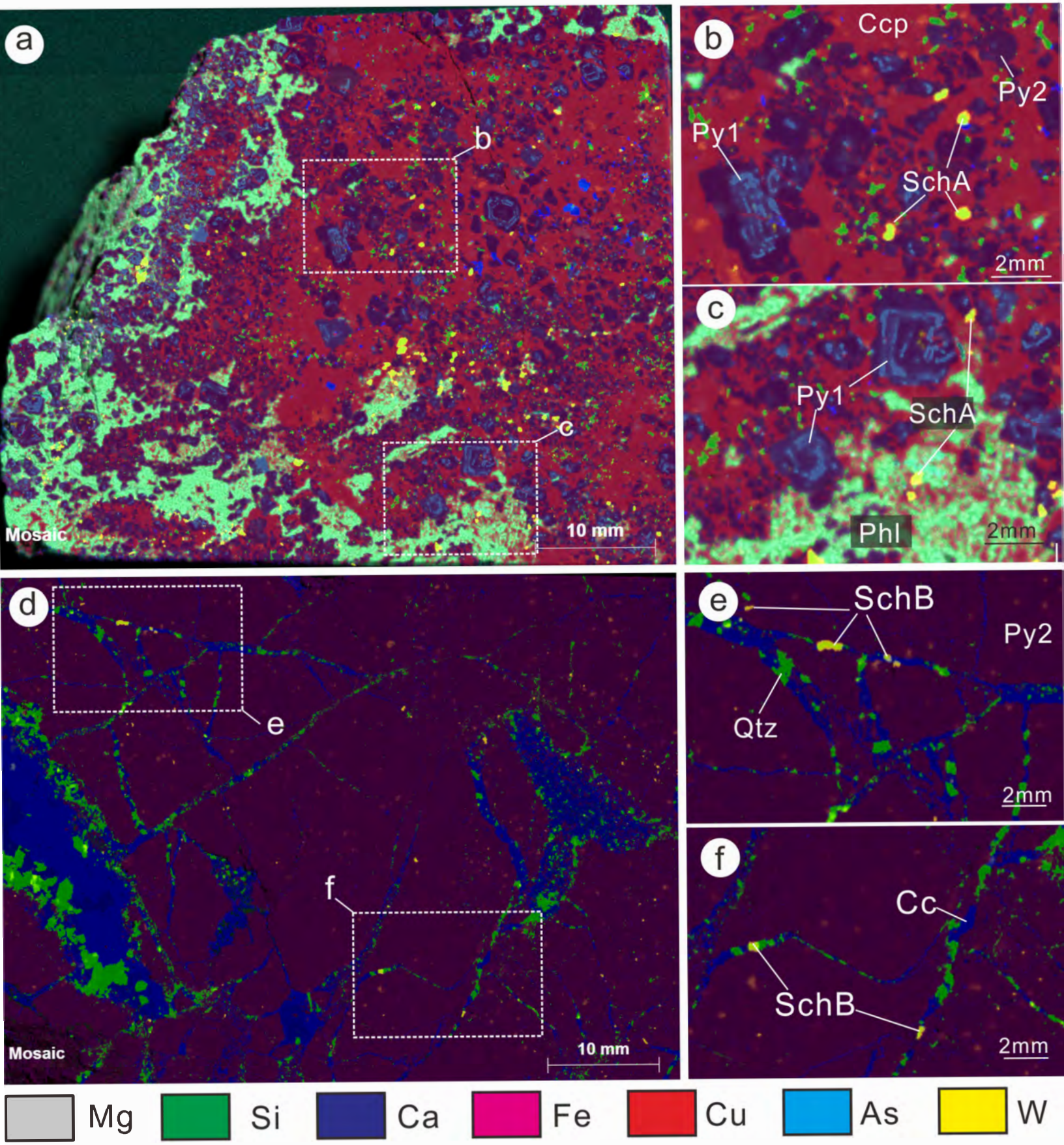
a
b
c
Mosaic
10 mm
b
Ccp
Py2
Py1
SchA
2mm
c
Py1
SchA
Phl
2mm
d
e
f
Mosaic
10 mm
e
SchB
Py2
Qtz
2mm
f
Cc
SchB
2mm
Mg
Si
Ca
Fe
Cu
As
W

Figure 5

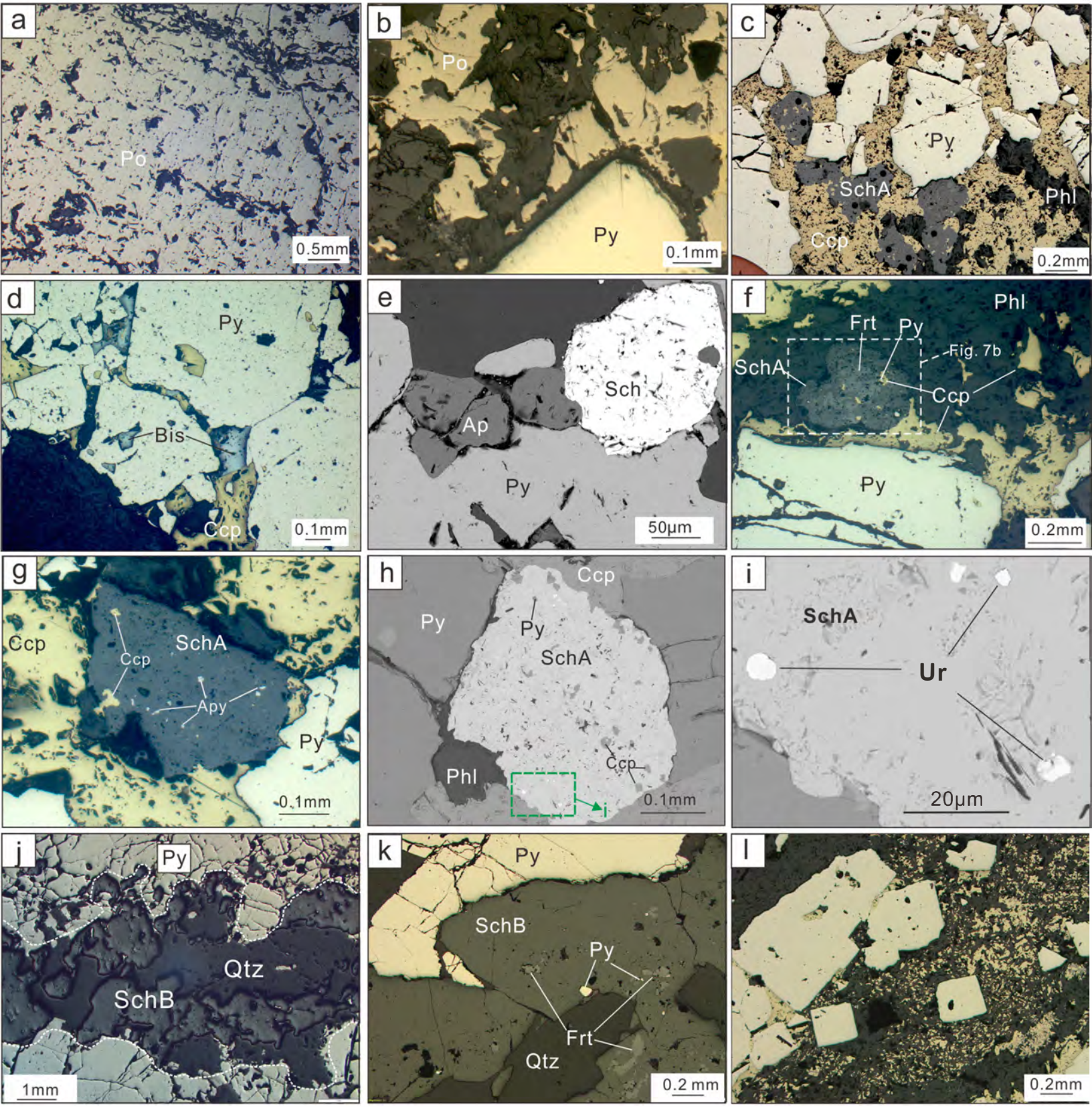
a
Po
0.5mm
b
Po
Py
0.1mm
c
Py
SchA
Phl
Ccp
0.2mm
d
Py
Bis
Ccp
0.1mm
e
Sch
Ap
Py
50μm
f
Phl
Frt
Py
Fig. 7b
SchA
Ccp
Py
0.2mm
g
Ccp
SchA
Ccp
Apy
Py
0.1mm
h
Ccp
Py
Py
SchA
Phl
Ccp
i
0.1mm
i
SchA
Ur
20μm
j
Py
Qtz
SchB
1mm
k
Py
SchB
Py
Frt
Qtz
0.2 mm
l
0.2mm

Figure 6

Minerals	Early-stage mineralization	Cu-(W) mineralization	Late-stage mineralization
Pyrrhotite			
Pyrite	Py1 Py2		
Chalcopyrite			
Quartz			
Scheelite		SchA SchB	
Uraninite			
Ferberite			
Arsenopyrite			
Apatite			
Bismuthinite			
Calcite			
Fluorite			
Talc			
Phlogopite			

Figure 7

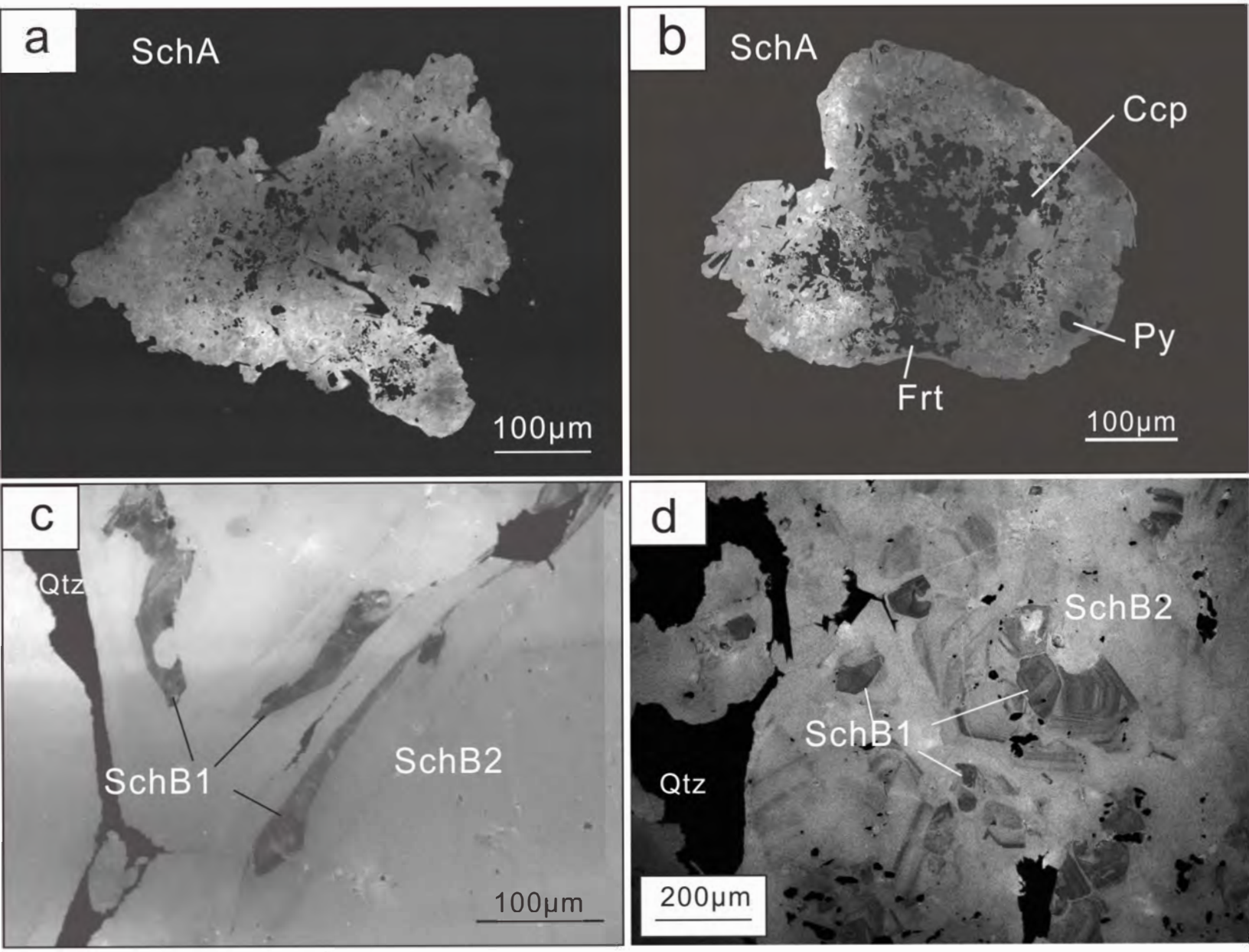
a
SchA
100μm
b
SchA
Ccp
Py
Frt
100μm
c
Qtz
SchB1
SchB2
100μm
d
SchB2
SchB1
Qtz
200μm

Figure 8

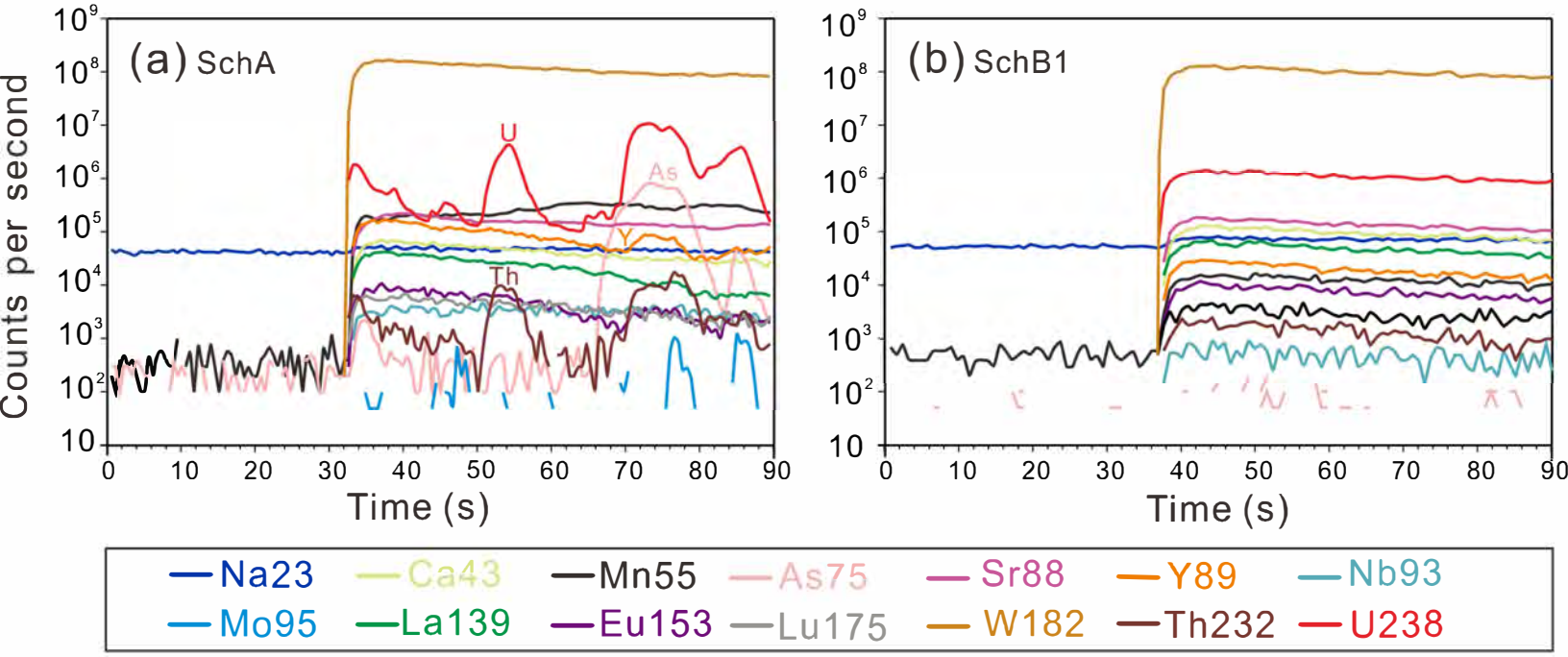
(a) SchA
(b) SchB1
Counts per second
Time (s)
U
As
Y
Th
Na23
Ca43
Mn55
As75
Sr88
Y89
Nb93
Mo95
La139
Eu153
Lu175
W182
Th232
U238

Figure 9

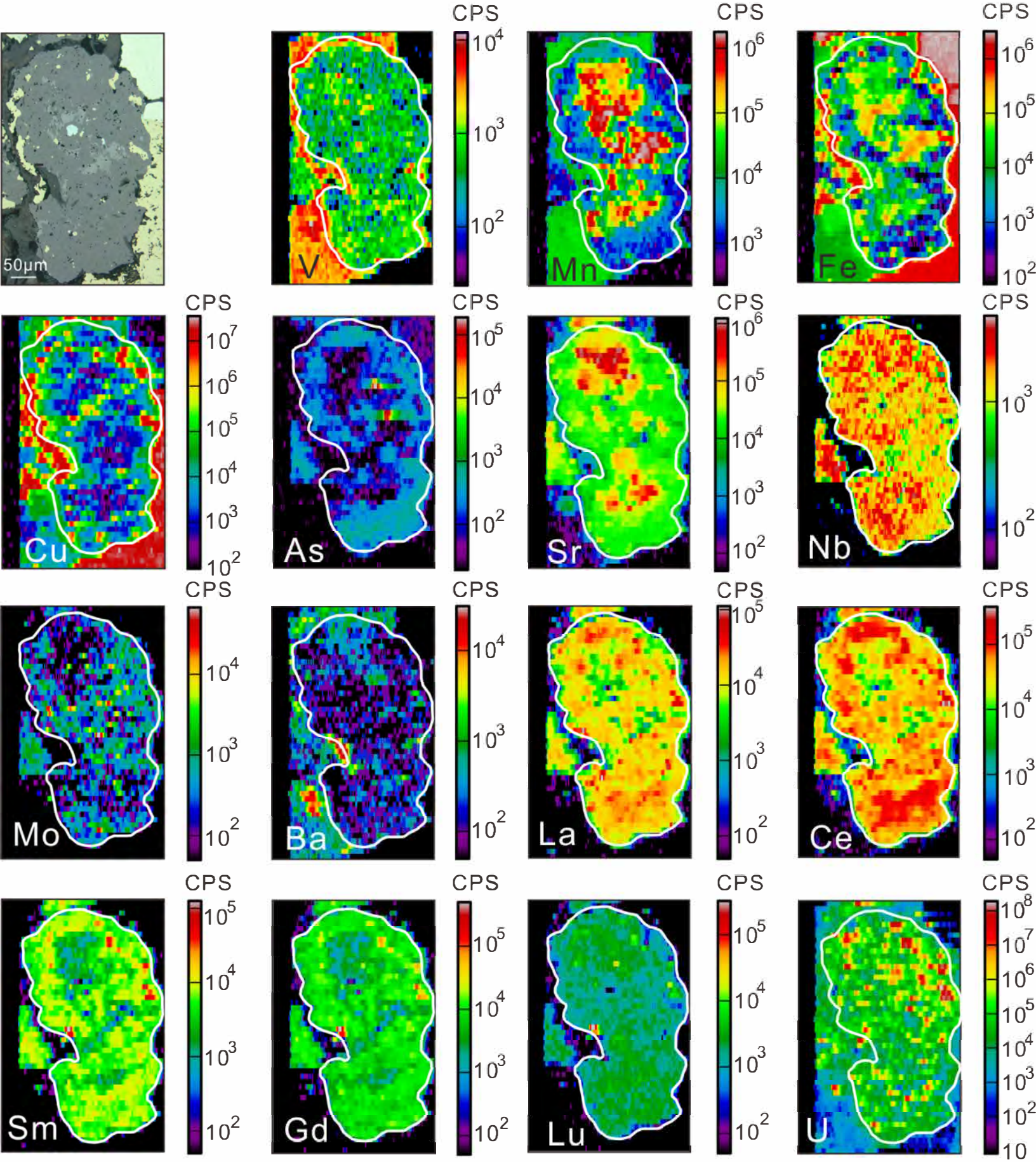

Figure 10

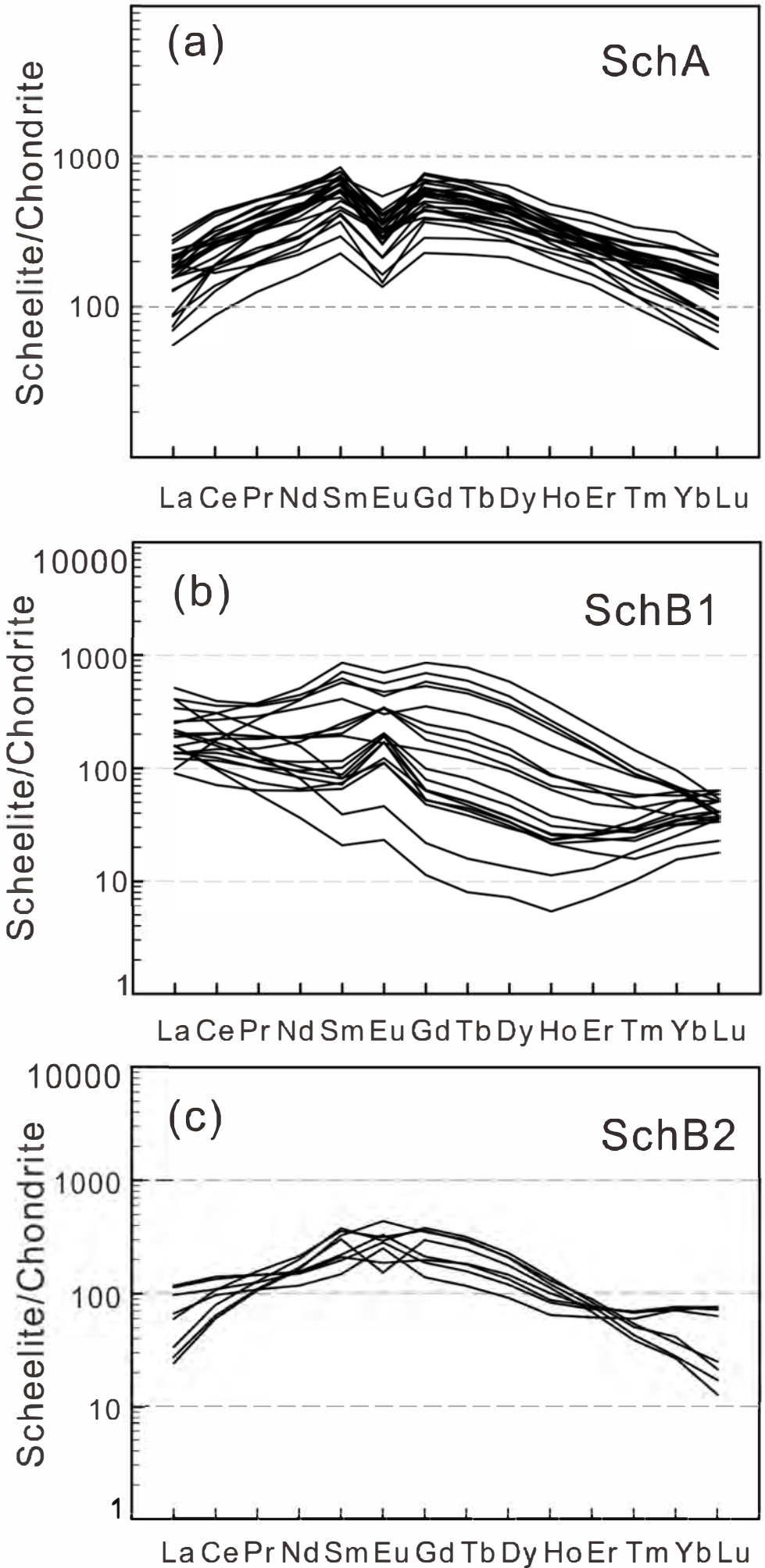
(a)
SchA
Scheelite/Chondrite
1000
100
La Ce Pr Nd Sm Eu Gd Tb Dy Ho Er Tm Yb Lu
(b)
SchB1
Scheelite/Chondrite
10000
1000
100
10
1
La Ce Pr Nd Sm Eu Gd Tb Dy Ho Er Tm Yb Lu
(c)
SchB2
Scheelite/Chondrite
10000
1000
100
10
1
La Ce Pr Nd Sm Eu Gd Tb Dy Ho Er Tm Yb Lu

Figure 11

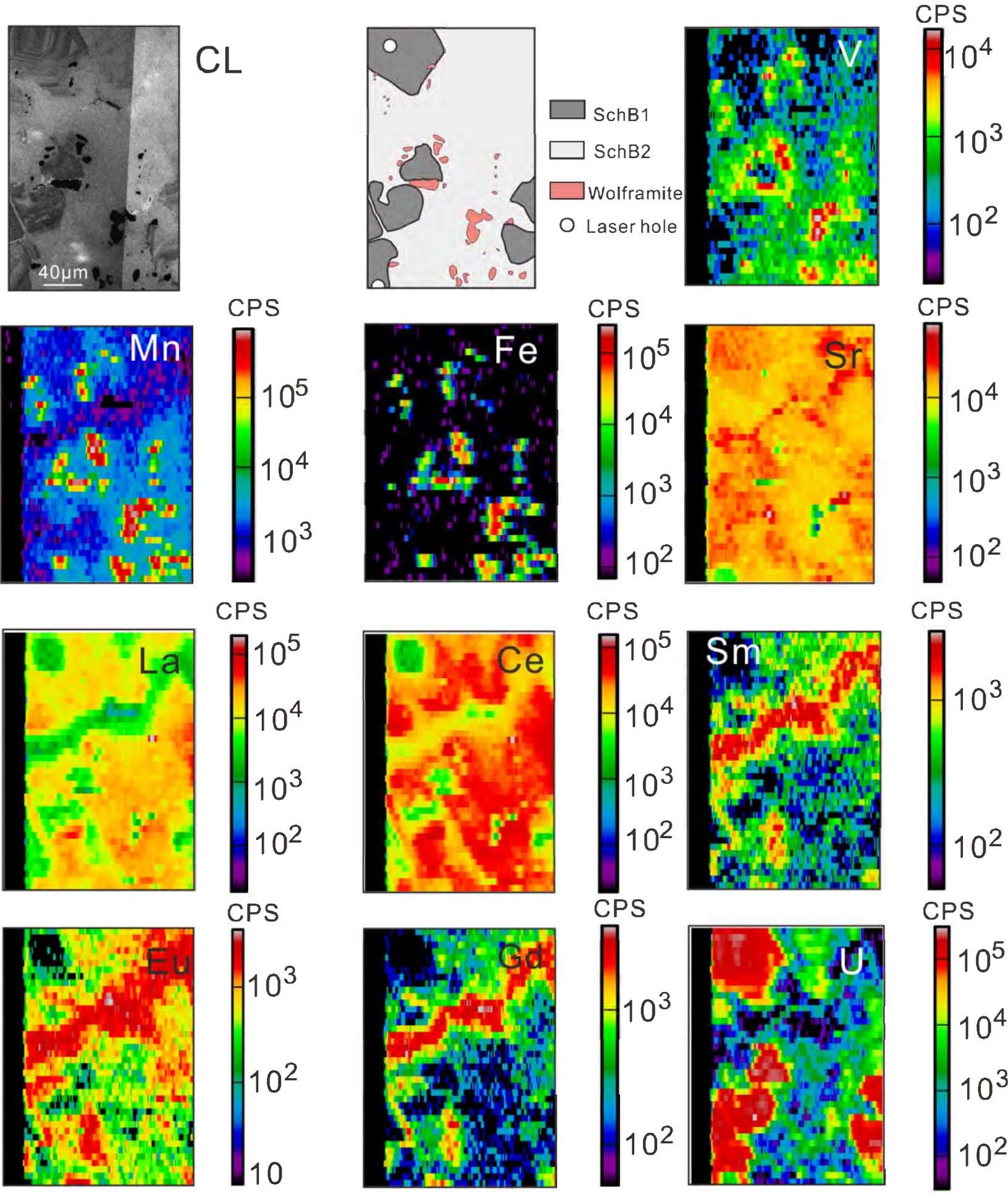
CL
40μm
SchB1
SchB2
Wolframite
Laser hole
V
Mn
Fe
Sr
La
Ce
Sm
Eu
Gd
U
CPS
10^5
10^4
10^3
10^2
10

Figure 12

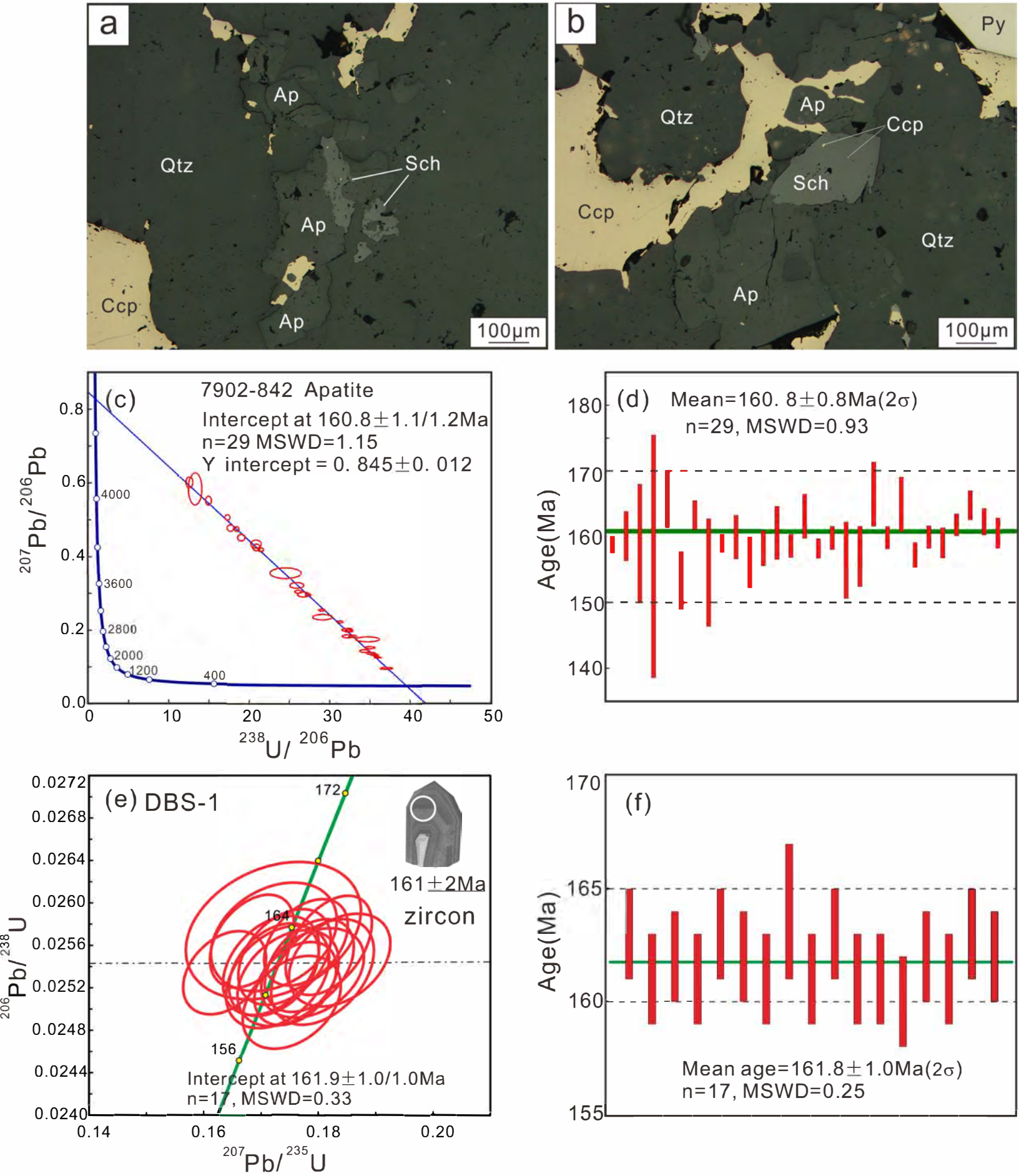
a
Ap
Qtz
Sch
Ap
Ccp
Ap
100μm
b
Py
Qtz
Ap
Ccp
Sch
Ccp
Qtz
Ap
100μm
(c)
7902-842 Apatite
Intercept at 160.8±1.1/1.2Ma
n=29 MSWD=1.15
Y intercept = 0. 845±0. 012
4000
3600
2800
2000
1200
400
207Pb/206Pb
238U/ 206Pb
(d)
Mean=160. 8±0.8Ma(2σ)
n=29, MSWD=0.93
Age(Ma)
(e) DBS-1
172
164
156
161±2Ma
zircon
Intercept at 161.9±1.0/1.0Ma
n=17, MSWD=0.33
206Pb/238U
207Pb/235U
(f)
Age(Ma)
Mean age=161.8±1.0Ma(2σ)
n=17, MSWD=0.25

Figure 13

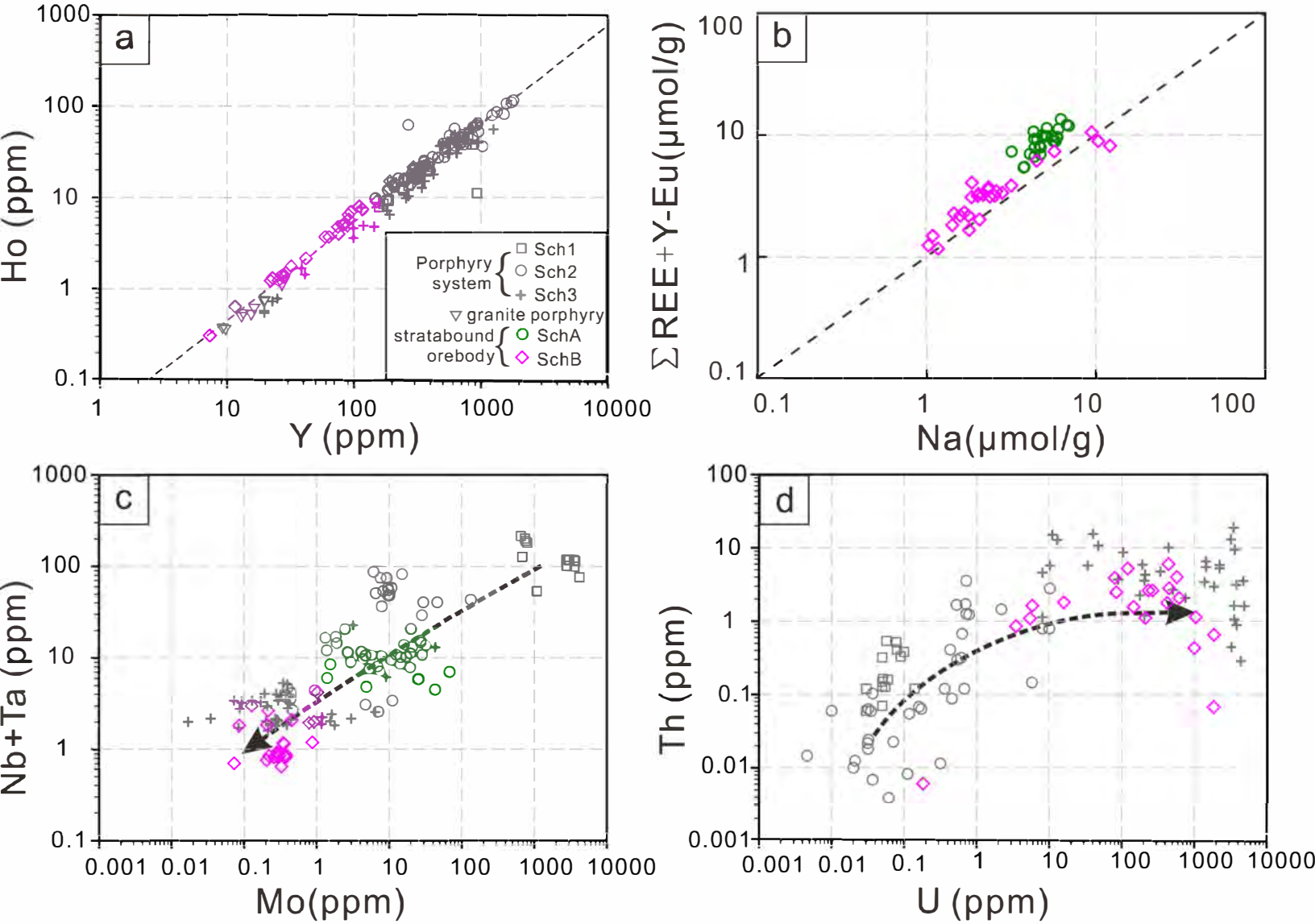
a
Ho (ppm)
Y (ppm)
Porphyry system
Sch1
Sch2
Sch3
granite porphyry
stratabound orebody
SchA
SchB
b
∑REE+Y-Eu(μmol/g)
Na(μmol/g)
c
Nb+Ta (ppm)
Mo(ppm)
d
Th (ppm)
U (ppm)

Figure 14

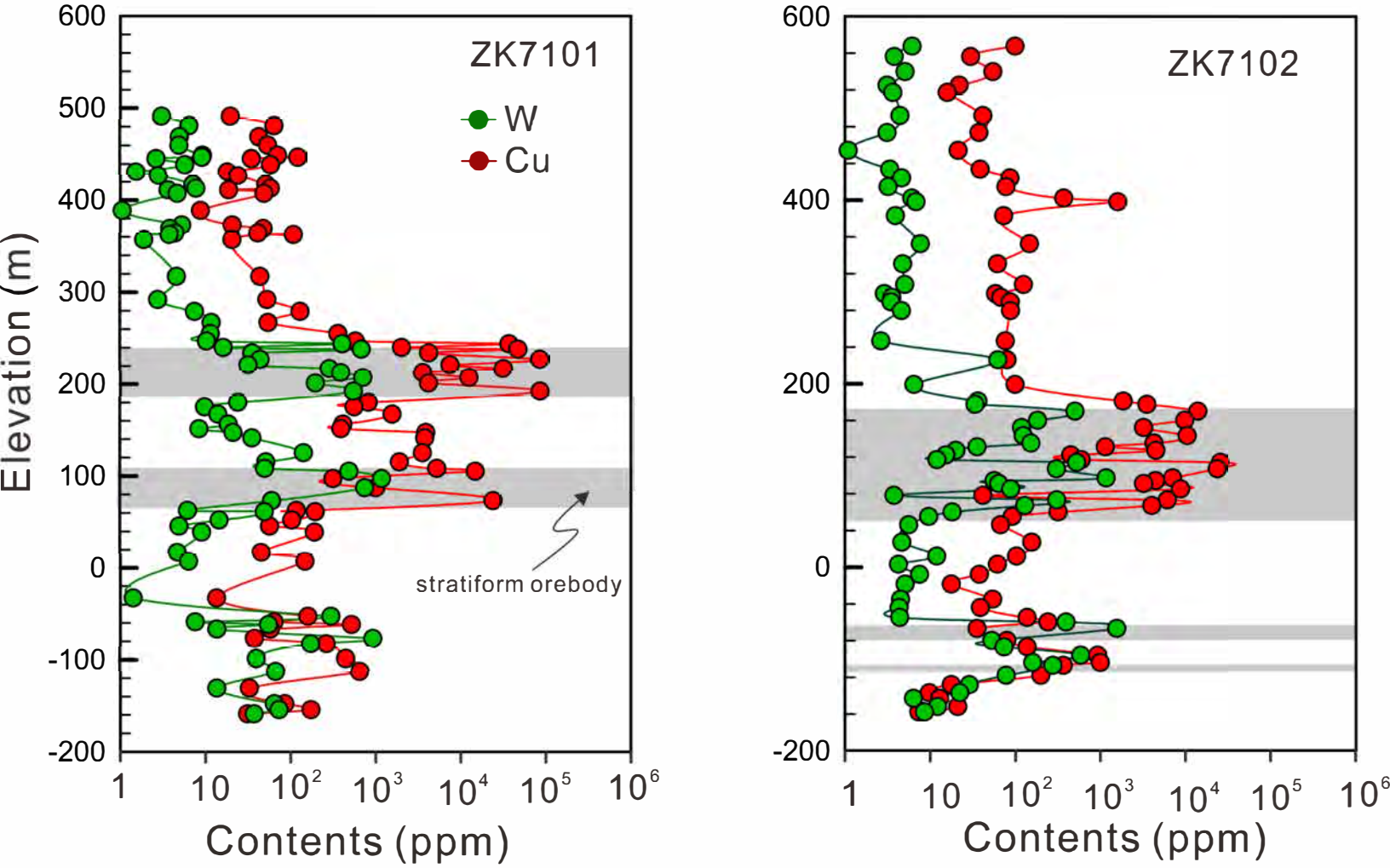
ZK7101
W
Cu
stratiform orebody
Elevation (m)
Contents (ppm)
ZK7102
Contents (ppm)